ETH Zürich

Master Thesis

A Novel Approach to Single Ion Addressing by means of a Multicore Photonic Crystal Fibre

Author:
John McCann

Supervisors:
Prof. Jonathan Home
Dr. Joseba Alonso

July 30, 2018

Acknowledgements

In the first instance I should like to thank Prof. Jonathan Home for giving the the opportunity to undertake my Master project in his TIQI group and for the support he gave me at every stage of the process. I hadn't hoped for a more insightful and interesting project, which, without the TIQI group, would not have been possible. I would thank Dr. Joseba Alonso for proposing the project to me and likewise for his extensive advice and guidance throughout the project. I thank Robin Oswald and Roland Matt for their work in the larger eQual project and for their frequent suggestions during my preparations and experiments, and their great help in producing this thesis. I further would like the aforementioned for their considerable patience and support through the period of my absence from, and return to, my studies.

I should like to thank Dr. Vlad Negnevitsky for his help with electronics, Dr. Frieder Lindenfelser and Prof. Lucas Novotny for their advice in building a system of lenses for single ion addressing and Dr. Michael Frosz for his provision of a photonic crystal fibre and advice on how to work with it.

Of course I am eternally grateful to my family for their unconditional support through everything I have ever done.

Contents

Chapter 1

Introduction

It has been some decades since the use of quantum systems in information processing was first proposed [1]. Since then numerous algorithms have been proposed making use of quantum information processing (QIP) that provide significant improvements over classical algorithms for certain problems [2]. Exponential improvements in processing time would in principle enable a quantum computer to perform tasks beyond the reach of any practical classical computer [3].

Recent industrial and research advancements, now including quantum computers with many tens of qubits [4, 5], have furthered technical and popular interest in the field. Several potential architectures are proposed and are under active investigation, such as superconducting qubits [6], trapped ions [7] or NMR [8]. In the TIQI group at ETH Zürich, work is done using trapped ions [9, 10].

1.1 Requirements for Quantum Information Processing

In this section I give a description of the use of trapped ions for quantum information processing, thus explaining the goal of single ion addressing and how this thesis fits into the overall project, and giving results that I will use later in this thesis.

In classical computation, information is stored as bits, where a single bit takes a value of either 0 or 1. Logical operations performed on these bits form the basis of information processing. Quantum computation extends the notion of a bit to a quantum bit, or qubit [11]. A single qubit is some two level quantum system defined by two orthonormal basis states $|0\rangle$ and $|1\rangle$ such that the general qubit state $|\psi\rangle$ is given by

$$|\psi\rangle = \cos\left(\frac{\theta}{2}\right)|0\rangle + e^{i\phi}\cos\left(\frac{\theta}{2}\right)|1\rangle \tag{1.1}$$

where $0 \leq \theta \leq \pi$ and $0 \leq \phi \leq 2\pi$. For use in quantum computing, any physically realised qubit must meet the DiVincenzo criteria [12]. These criteria can be summarised as a physical quantum computer having

1. A scalable collection of well characterised qubits
2. The ability to initialise the qubits into a known state
3. Long coherence times compared to the gate timescales
4. A universal set of quantum gates
5. The ability to measure individual qubit states

1.2 Trapped Ion Qubits

In this section, I look at the use of trapped $^{40}\mathrm{Ca}^+$ ions. Previously, work has been done in the TIQI group using the Optical qubit of $^{40}\mathrm{Ca}^+$ [13], with the qubit transition at 729 nm. In the future eQual experiment, it is planned to use the Zeeman qubit [14], controlled by a Raman transition at 400 nm. Working as part of

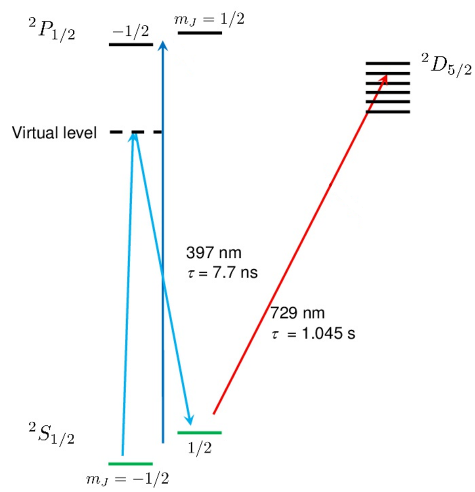

Figure 1.1: The $^2S_{\frac{1}{2}}$ states $|m_J = \pm\frac{1}{2}\rangle$ are taken as the qubit states $|0\rangle$ and $|1\rangle$. Transitions between these gates can be driven by a Raman transition at 400 nm via a virtual state detuned from the $^2P_{\frac{1}{2}}$ states. The rapid decay of $^2P_{\frac{1}{2}}$ gives fluorescent light for imaging, enabling the qubit states to be distinguished by shelving one state in a $^2D_{\frac{5}{2}}$ state. Image by M. Zeyen [15].

the eQual project, it is therefore this second option that I consider in this report. An energy level diagram for this ion is given in figure 1.1.

The Zeeman qubit is defined with the $^2S_{\frac{1}{2}}$ states to satisfy criterion 1. In this presence of some magnetic field, these states are split and can be used so that the lower energy state $|m_J = -\frac{1}{2}\rangle \equiv |0\rangle$ and the higher energy state $|m_J = +\frac{1}{2}\rangle \equiv |1\rangle$. This qubit has decay time of 10^6 years and in a stable magnetic field can have a long coherence time [16] of 2.1 s and so criterion 3 is satisfied. The qubit basis states can be made to fluoresce under light at 397 nm by repeatedly exciting them to the $^2P_{\frac{1}{2}}$ states and having them decay back. By first shelving the $|1\rangle$ state into some metastable state such as $^2D_{\frac{5}{2}}$ by a transition at 729 nm, only ions in the $|0\rangle$ will fluoresce in this way. By collecting the photons emitted by the decay, the two states can be distinguished achieving criterion 5. By sideband cooling [17], and pumping through the $^2P_{\frac{1}{2}}$ state, ions can be initialised into both their motional and qubit ground states, thus satisfying criterion 2. Finally, the performance of quantum gates for criterion 4 requires being able to drive the transition between the $|0\rangle$ and $|1\rangle$ states. This can be done by driving a Raman transition [18] via a virtual level detuned by some detuning Δ from the $^2P_{\frac{1}{2}}$ states. The Rabi frequency [18] of such a transition is given by

$$\Omega_{\text{Raman}} = \frac{\Omega_0 \Omega_1^*}{2\Delta} \tag{1.2}$$

where Ω_0 and Ω_1 are the Rabi frequencies for the transitions between the virtual state and the $|0\rangle$ and $|1\rangle$ states respectively, given by

$$\Omega_i = \left\langle virtual \left| \frac{e}{\hbar} \vec{r} \cdot \vec{E}^{(i)}(\vec{r}) \right| i \right\rangle \tag{1.3}$$

where $\vec{E}^{(i)}(\vec{r})$ are sinusoidally oscillating electric fields, such as that provided by a laser, with frequencies corresponding to the energy difference between the states. The Raman transition time can in principle be reduced by decreasing Δ at a cost of risking photons scattering from the $^2P_{\frac{1}{2}}$ state. Hereafter I assume a value of $\Delta = 3$ nm and therefore two Raman beams at close to $\lambda = 400$ nm. Assuming that the two Raman fields $\vec{E}^{(i)}(\vec{r})$ have the same amplitudes $\vec{E}^{(0)}(\vec{r}) = \vec{E}^{(1)}(\vec{r}) = \vec{E}(\vec{r})$, and that the spatial variation of this amplitude is small over the volume of an ion, we can see that

$$\Omega_{\text{Raman}} \propto |\vec{E}(\vec{r})|^2 \propto I(\vec{r}) \tag{1.4}$$

where $I(\vec{r})$ is the intensity and $\vec{r}$ is the location of the ion within the field.

Such Raman transitions can be used to drive single qubit gates. Multiple ions, each carrying a single qubit, can be contained within a single trap and additional lasers can be used couple between the internal states of ions and their motional states within the potential well, allowing for two-qubit gates [11]. In this way, a universal set of gates can be generated.

A linear ion trapped can trap several ions in a string, typically separated by a few micrometres. In general for multiple ions, the spacing between ions is not equal [19] due to their mutual electrostatic repulsion, but with segmented trap electrodes, the trapping potential can be deformed to allow for equally spaced ions. For this thesis I assume 7 trapped ions, spaced equally by 5 µm. Ideally, single qubit gates being performed on a single ion would occur independently, meaning that the field intensity at an ion could be turned on without any increase in intensity at other ions. This is what is meant by Single Ion Addressing. In practice it is impossible to achieve this perfectly, as the electric field of a laser beam is in principle infinite in extent, and the effect on one ion of driving a transition in another ion is crosstalk. Protocols exist to reduce the effect of, or correct the errors due to, crosstalk but an acceptable threshold for crosstalk is to have a ratio between the intensity at an ion, and at a neighbouring ion, of 10^{-4} [20].

1.3 An Outline of this Thesis and its Goals

Thus the goal of this thesis concerns criteria 4 and 5. A system must be designed that allows for single ion addressing, delivering controllable, high optical intensity beams to the trapped $^{40}\text{Ca}^{+}$ ions to drive single qubit transitions in individual ions quickly, with acceptable crosstalk. It must also allow for single ion measurement, collecting fluorescent light from ions to allow their state to measured, and the light from each ion to be distinguished.

Such a thing has been achieved before, for example, [21, 22] makes use of a multi-channel acousto-optic modulator (AOM), separated from the ions by a single lens which focuses the multiple beams from each channel onto each ion individually. More optics placed above the ions are then used for imaging. Alternatively in [23], the same objective lens was used for both imaging and addressing, with the light for each superimposed using a dichroic, and only a single beam addressing each ion in turn, directed by a single AOM.

Here we try what we believe to be a novel approach. We hope to achieve single ion addressing using multiple beams, controlled individually by AOMs before being brought together into the cores of a Multicore Photonic Crystal Fibre (MC-PCF). The other end of the MC-PCF can then be mounted into a system of optics which simultaneously will focus all beams, with each one being focused onto a single ion. The same objective lens is then used to collect fluorescent light for imaging, which is then separated from the addressing beams by a dichroic mirror.

Such a system would allow simultaneous addressing of many single ions, one by each of the many beams. The use of a MC-PCF allows the many beams to be very close together, with a large degree of overlap everywhere except at the endface of the MC-PCF and at the ions. This allows all beams to be equally focused by the system of addressing lenses. We also hope that it is well scalable. In this project we use 7 cores of an MC-PCF, for 7 ions that together, for example, might constitute a logical qubit, but in principle the method could be scaled to an MC-PCF with many more cores, addressing more ions.

Figure 1.2 depicts the overall plan, and also gives a guide for the structure of this thesis. I attempt to address in turn every stage of a beam of light, as it progresses from a laser source, to the ions, and to an imaging detector. In this way I hope to inform anyone who might have looked at my experiments what was happening at every position, and inform anyone who might use the equipment again in future.

In chapter 2 I discuss the basics of Gaussian beams, such as those typically produced from lasers or optical fibres. I describe a laser that was bought from M Squared Lasers, producing light at the wavelength $\lambda = 400\,\text{nm}$ for controlling the Zeeman qubit. I describe some prelimary tests I performed, and steps I took to make the beam ready for later use.

In chapter 3 I describe how the single beam was divided into the 7 beams that will eventually reach the ions, and controlled by AOMs. I discuss different ways of achieving this, explaining why an in-fibre solution

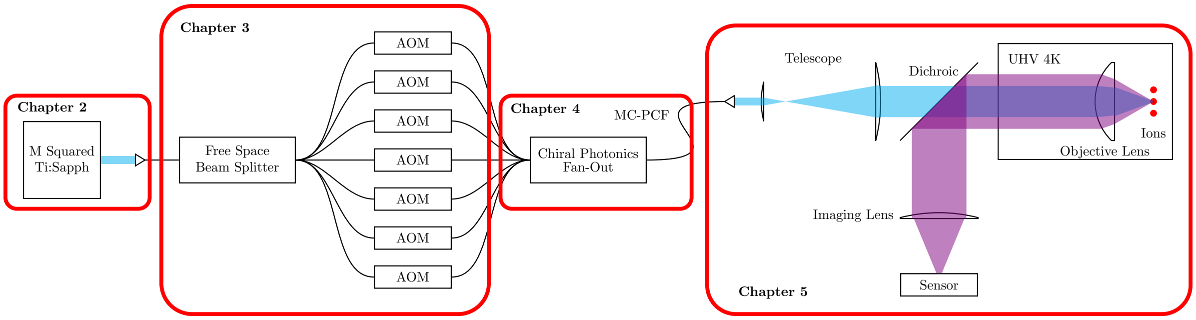

Figure 1.2: In successive chapters of this project, I follow the path of a beam of light, from the Laser, through a Beamsplitter and AOMs, into an MC-PCF, and finally through a system of lenses to an ion trap, demonstrating in the process the potential for single ion addressing and imaging.

was not possible, describing and characterising a relatively efficient freespace beamsplitter I built, that might easily be scaled for more qubits.

In chapter 4 I examine the MC-PCF that we acquired. I give a theoretical overview of photonic crystal fibres, and I characterise the beams that can be by produced our fibre. I find a way to couple the light coming from the AOMs into the MC-PCF and discuss a notable loss mechanism, photodarkening, that occurs as part of this process.

In chapter 5 I cover the goals and constraints that the single ion addressing system must achieve. I design and simulate a system of lenses that can achieve single ion addressing and imaging with tight beam focusing and acceptable crosstalk. I build and characterise this system and try to explain why it didn't work as expected.

Finally, in chapter 6 I summarise and conclude the work that I did, discuss what worked and what did not, and say further work can be done and what work is planned for the future.

Chapter 2

Laser

In this chapter I discuss a laser that was acquired for use in future quantum information processing experiments. In section 2.1 I summarise the equations that govern Gaussian beam propagation, which inform the work I do in subsequent chapters, and which will be referred to throughout this report. In section 2.2 I describe the laser in question that was purchased from M2, giving its key features. Finally in section 2.2.1 and 2.2.2 I perform some preliminary tests on this laser, looking to see where its beam differs slightly from a desirable beam, and some corrections that I did that remain in place in my subsequent work.

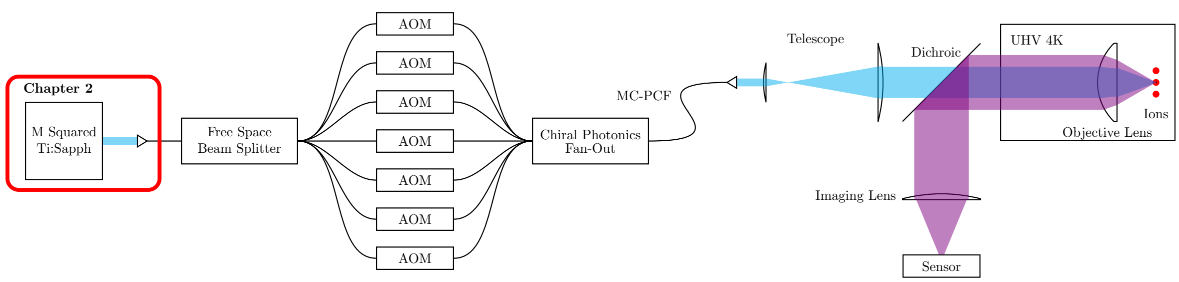

Figure 2.1: In Chapter 2 I describe the laser used in later chapters, and the preliminary tests I did with it.

2.1 Gaussian Beams

A review of the theory of Gaussian optics would be informative here and will be useful again in later sections. In this section I will outline the theoretical origins of Gaussian beams and give statements of their key properties which will be referred to through much of the remainder of this report. Detailed derivations of these results can be found, for example, in [24]. Typically a light beam produced by a laser or from the end of an optical fibre is a good approximation to a Gaussian beam and so understanding the nature of such a beam is important to their use.

If optics is the study of the propagation of electromagnetic radiation, naturally any theoretical investigation begins from the wave equation. For the electric field $\vec{E}(x, y, z, t)$ propagating in free space this is

$$\left(c^2\vec{\nabla}^2 - \frac{\partial^2}{\partial t^2}\right)E(x, y, z, t) = 0 \tag{2.1}$$

Of course, in the interesting case of a wave with frequency ω propagating in some direction $\vec{z}$ this is separable into spatially and temporally varying components $\vec{E}(x, y, z, t) = \vec{x}E(x, y, z)e^{-i\omega t}$, where $\vec{x}$ is some axis orthogonal to $\vec{z}$, this can be reformulated as the Helmholtz equation

$$\left(\nabla^2 + k^2\right)E(x,y,z) = 0 \tag{2.2}$$

We can separate the spatial variation into a rapid oscillation along $\vec{z}$ of wavevector $k = \frac{\omega}{c} = \frac{2\pi}{\lambda}$ and a spatial envelope $U = U(x,y,z)$ such that $E(x,y,z) = U(x,y,z)e^{-ikz}$. In the slowly varying envelope approximation

$$\frac{\partial^2 U(x,y,z)}{\partial z^2} \ll k\frac{\partial U(x,y,z)}{\partial z} \tag{2.3}$$

we can write an equation for the envelope

$$\left(\frac{\partial^2}{\partial x^2} + \frac{\partial^2}{\partial y^2} - 2ik\frac{\partial}{\partial z}\right)U(x,y,z) = 0 \tag{2.4}$$

Finally we can try to separate the solution, for a suitable choice of axes x and y, such that $U(x,y,z) = U_x(x,z)U_y(y,z)$, and we see that each part obeys a similar equation, which for the x component is

$$\left(\frac{\partial^2}{\partial x^2} - 2ik\frac{\partial}{\partial z}\right)U_x(x,z) = 0 \tag{2.5}$$

This equation admits many modes of solution, given generally by

$$U_x(x,z) \propto \left(\frac{\omega_0}{\omega(z)}\right)^{\frac{1}{2}} H_m\left(\sqrt{2}\frac{x}{\omega(z)}\right)e^{-\frac{x^2}{\omega(z)}}e^{-\frac{ikx^2}{2R(z)}}e^{(m+\frac{1}{2})i\psi(z)} \tag{2.6}$$

where $H_m(x)$ is the mth Hermite polynomial, and the beam radius $\omega(z)$, wavefront radius $R(z)$ and Gouy phase $\psi(z)$ parameterise a specific beam as we will interpret shortly. They vary along the beam according to

$$\omega(z) = \omega_0\sqrt{1 + \left(\frac{z}{z_R}\right)^2} \tag{2.7}$$

$$R(z) = z\left(1 + \left(\frac{z_R}{z}\right)^2\right) \tag{2.8}$$

$$\psi = \tan^{-1}\left(\frac{z}{z_R}\right) \tag{2.9}$$

where the Rayleigh length z_R is given by

$$z_R = \frac{\pi\omega_0^2}{\lambda} \tag{2.10}$$

We stress at this point that a beam is generally astigmatic, so each of these parameters is specific to the solution for $U_x(x,z)$ and may all in general differ for $U_y(y,z)$, including the choice of origin of the z axis such that $z_x = z_y + \Delta z$. Given these results, we can write the lowest order solution $m_x = m_y = 0$ of equation 2.4, known as the Gaussian mode

$$U(x,y,z) = E_0\prod_{a=x,y}\sqrt{\frac{\omega_{0a}}{\omega_a(z_a)}}e^{-\frac{a^2}{\omega_a(z_a)^2}}e^{-ik\frac{a^2}{2R_a(z_a)}}e^{\frac{i}{2}\psi(z_a)} \tag{2.11}$$

It is also worth noting at this point that power intensity $I \propto |E|^2$ of the beam has a comparably simple expression

$$I(\vec{r}) = I_0\prod_{a=x,y}\frac{\omega_{0a}}{\omega_a(z_a)}e^{-\frac{2a^2}{\omega_a(z_a)^2}} \tag{2.12}$$

or in the desirable case of $\omega_{0x} = \omega_{0y}$ and $\Delta z = 0$

$$U(x,y,z) = E_0\frac{\omega_0}{\omega(z)}e^{-\frac{r^2}{\omega(z)^2}}e^{-ik\frac{r^2}{2R(z)}}e^{i\psi(z)} \tag{2.13}$$

$$I(x,y,z) = \frac{2P}{\pi\omega\left(z\right)^2} e^{-\frac{2r^2}{\omega(z)^2}} \tag{2.14}$$

where E_0 is the maximum electric field amplitude, P is the total power in the beam, and $r^2 = x^2 + y^2$ the radial coordinate. Given a solution of this form, we can see some key properties of a Gaussian beam that will be referred to later throughout this report. It is instructive to consider these in both the near field, close to $z = 0$ and in the far field regime where $z \gg z_R$.

Of course the electric field amplitude is everywhere non-zero, but in the the first exponential term, we see that it's amplitude forms a Gaussian envelope. The parameter $\omega(z)$ defined in equation 2.7 is characteristic of the beam radius at a position z, such that at $r = \omega(z)$ the electric field amplitude falls to $\frac{1}{e}$ of its value at $x = 0$, or equivalently, that the intensity falls to $\frac{1}{e^2}$. Thus we see that 96% of the total power is contained within a circle centred on the z axis with radius ω.

Considering the near field regime $z < z_R$, we see that the beam comes to its narrowest point $z = 0$, where $\omega = \omega_0$. At the origin $x = y = z = 0$ of such a beam, where the beam is most tightly focused, the global maximum of the electric field amplitude is found and likewise the point of highest intensity, with the maximum intensity $I_{\max} \propto {\omega_0}^{-2}$. At this point we may also interpret the quantity z_R, the Rayleigh length, defined in equation 2.10. It is characteristic of the length of this tightly focused, high intensity region. At $z = z_R$, the beam radius $\omega(z)$ has increased by a factor of $\sqrt{2}$ and the on-axis intensity has fallen by a factor of 2. We notice in general from the factor under the square root that the on axis field strength follows a Lorentzian distribution.

In the far field $z \gg z_R$, the expression given in equation 2.7 reduces to

$$\omega(z \gg z_R) = \frac{\omega_0}{z_R} z = \frac{\lambda}{\pi\omega_0} z \tag{2.15}$$

We see that the surface around the z axis defined by ω tends to a cone, defined by the divergence angle

$$\theta = \frac{\lambda}{\pi\omega_0} \tag{2.16}$$

Again, within this cone propagates 96% of the beams total power. Important to note is the inverse relationship between the divergence angles and the size ω_0 of the beam at its narrowest point. Thus a more tightly focused beam necessarily converges or expands more rapidly. The Gaussian mode given in equation 2.13 optimises this relationship. Higher order modes present in physical beams diverge more rapidly than this. As such we can define a pragmatic value M^2 such that

$$\theta = \frac{\lambda}{\pi\omega_0} M^2 \qquad M^2 = \frac{\theta_{\text{measured}}}{\theta_{\text{ideal}}} \tag{2.17}$$

where θ and ω_0 are now defined such that the far field cone and near field waist are where the measured value of the electric field amplitude falls to $\frac{1}{e}$ or the intensity falls to $\frac{1}{e^2}$.

Considering now the second exponential factor in equation 2.13, we see that it introduces a phase shift in the beam, and thus a shift in the position of wavefronts, relative to its value on the z axis. As such we can interpret the factor $R(z)$ as the radius of curvature of the wavefronts close to the axis. Again, looking at the beam close to the origin, we see that the in the near field region, $R \to \infty$ and so the beam approximates a plane wave. Likewise, in the far field region, $R \to z$ and so the wavefronts approximate those of a spherical wave centred on the origin.

2.2 M Squared Laser at 400 nm

In section 1.2 I described more fully the nature of the experimental setup that is planned for future. Here, I will say only that a core requirement of trapped ion quantum information processing is the ability to drive a transition between the two energy states of an ion that form a qubit. This has previously been done using an optical transition at 729 nm, but in future it is intended to use a Raman transition at 400 nm. Transitions are driven by an oscillating electric field, such as that produced by a laser, at the requisite frequency.

Lobe Order	Power mW	Power %
3	0.2	0.6
2	0.7	2.0
1	2.5	7.3
0	31.0	90.1
Total	34.4	100

Table 2.1: Tabulated is the power contained in each side lobe order, as depicted in figure 2.2.

A titanium-sapphire laser [25] was acquired from M Squared, model number SolsTiS 5000 SRX F. It has a tunable wavelength range of 725 nm to 960 nm. Further, the ECD-x module was purchased, which contains a frequency doubling cavity giving a tunable output wavelength range of 385 nm to 415 nm. Frequency doubling is achieved by means of repeated passage of light through a non-linear crystal which leads to second-harmonic generation [26].

As such, we had a laser that could provide up to 2 W at the desired wavelength of 400 nm, and it is this option that I will consider for the remainder of the thesis. The option was retained to instead also perform experiments at 729 nm with 5 W. In principle, the output power could be controlled by varying the power from the pump laser, or could be distributed between the undoubled beam output and the doubler by using a half-waveplate and a polarising beam splitter, but it was found in practice that the doubling cavity didn't lock if the input power was lower than 50 %. Since, at least initially, very lower power of the order of mW would be used, for aligned and characterisation, I therefore would routinely deliver the maximum amount of power to the frequency doubling module, and then use additional waveplates and beamsplitters to reduce the power as desired, with the majority of the power being directed into a heatsink.

2.2.1 Side lobes measurement

The beam from the laser was found to have higher order lobes adjacent to the central mode. In order to measure the amount of the power in each lobe, I place a power metre in the path of the beam and in front of it an iris the diameter of which could be varied between blocking the beam entirely and allowing the whole beam to pass. Ensuring the central lobe of the beam was passing throught the centre of the iris, I progressively narrowed the iris, recording the power transmitted as each order of side lobe was excluded. In this way I saw that the vast majority of power was contained within the central Gaussian mode. The results are seen in table 2.1. Figure 2.2 shows schematically the profile of the beam, labelling the side lobes for clarity. In future experiments I used the iris to exclude all except the central, zeroth, lobe.

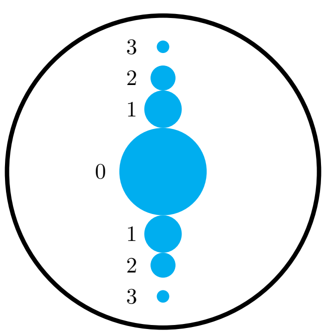

(a)

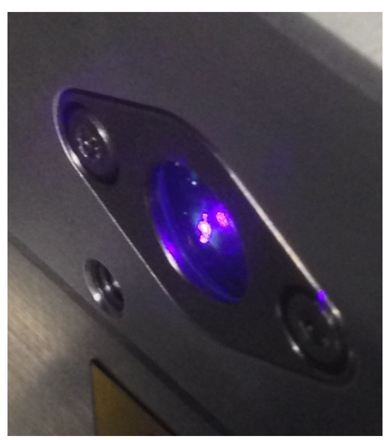

(b)

Figure 2.2: Figure 2.2a shows a schematic diagram of the beam profile, with the lobe order defined for table 2.1. Figure 2.2b depicts light scattered by the beam on the output window of the ECDx frequency doubling module, with the 0th and 1st order lobes visible.

2.2.2 Astigmatism

Ideally one would like to work with an initial beam that has both a low divergence and a low ellipticity and astigmatism. A low divergence is useful because it means the diameter of a beam will not vary greatly along its length. This gives flexibility in the position of any optical components that are subsequently placed in the beam. As seen in equation 2.15, a beam with a low divergence must necessarily have a large diameter. A larger diameter also has the effect of reducing the beam intensity, which has an additional bonus of not risking accidental damage to optical components or to my hands. A circular, unastigmatic beam is desirable because it has a single, circular, waist. This gives the highest possible beam intensity at the waist, allows for better efficiency optical fibre coupling, and allows the beam to be manipulated along both axes simultaneously using simple, spherical lenses.

After seeing the beam from the laser to diverge differently along axes perpendicular and parallel to the optical table, I used a beam profiler to measure the size of the beam at several positions along 750 mm of the beamline. The beam profiler had the ability to quickly display an estimate of the spot size at its detector along the 2 axes, which I recorded directly. The position along the beam line was measured by fixing the beam profiler at screwholes spaced at multiples of 25mm. Sequential measurements required the repeated removal and resecuring of the beam profiler. Mirrors were used to raise to the beam to a height appropriate for the beam profiler and to align it with the screwholes. A translation stage was used to adjust the beam profiler to more finely ensure the beam was centred on the sensor. The disturbance of moving the profiler would cause the ECD-X frequency doubler cavity to unlock and re-lock. I expect that slight differences in mirror positions inside the doubler account for the deviations from a smooth increase in beam size. The results are plotted in figure 2.3.

Fitting this to straight line I estimate the divergences parallel and perpendicular to the table respectively to be

$$\theta_x = 0.078(2)^\circ \qquad \theta_y = 0.036(2)^\circ \tag{2.18}$$

Assuming a high quality beam, close to $M^2 = 1$, it is possible to extrapolate the beam backwards and so to calculate a theoretical waist radius and position. I show a calculated beam radius in the x and y directions in figure 2.4. In the figure, the origin is the same as for figure 2.3, being the position along the beam where I started measuring. This position was determined by the availability of space on the table. Because the measurements required a long straight, unobstructed region, it was not possible measure all along the beam to the output of the laser. The red region of the plot extrapolates the beam inside the laser itself, and as such is unphysical. It does however allow the beam's astigmatism to be seen clearly and it can be used to show theoretical values of the waist positions and sizes.

I chose a pair of cylindrical lenses to alter the more quickly diverging x axis to bring it into alignment with the y axis, thus producing a circular unastigmatic beam. The lens were chosen to do this using a small amount of table space, by being close together and by being as close as possible to the laser output so as not to waste space. Using only a single lens would work only if placed at the point where the two directions had equal radii, coincidentally close to my chosen origin, which is far from the laser. I calculated the effects of various lenses using ray transfer analysis and found that a 30 mm focal length lens followed by a 70 mm focal length lens separated by 105 mm placed 426 mm closer to the laser than my origin would achieve the task to a satisfactory level. The corrected beam is also shown in figure 2.4 and clearly is well aligned with the y axis of the beam.

To decrease the new divergence of the beam altogether I then built various refracting telescopes of two convex lens spaced by the sum of their focal lengths using the simple relation [27]

$$\frac{f_1}{f_2} \approx \frac{\omega_1}{\omega_2} \tag{2.19}$$

It is for this reason that I chose to use cylindrical lenses to fix the astigmatism, rather than, for example, toroidal lens to focus the beam in both directions simultaneously. Toroidal lenses are somewhat more expensive than cylindrical lens, but given the reasonable possibility that the beam may later need to be expanded or contracted anyway, they provide no benefit over and less flexibility than the pair of telescopes I have described.

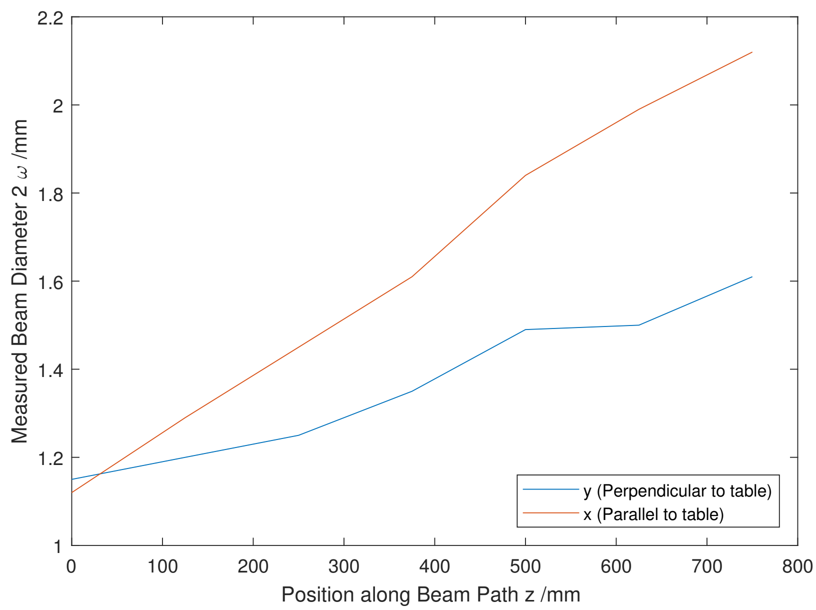

Figure 2.3: Shown is the measured size of the beam, as defined in equation 2.15. As expected, in the far field regime, the beam size grows linearly with distance, allowing θ to be estimated. The beam grows at different rates vertically and horizontally, and so is astigmatic according to equation 2.11. The origin is defined by the first available measurement position, being about 400 mm from the output of the laser.

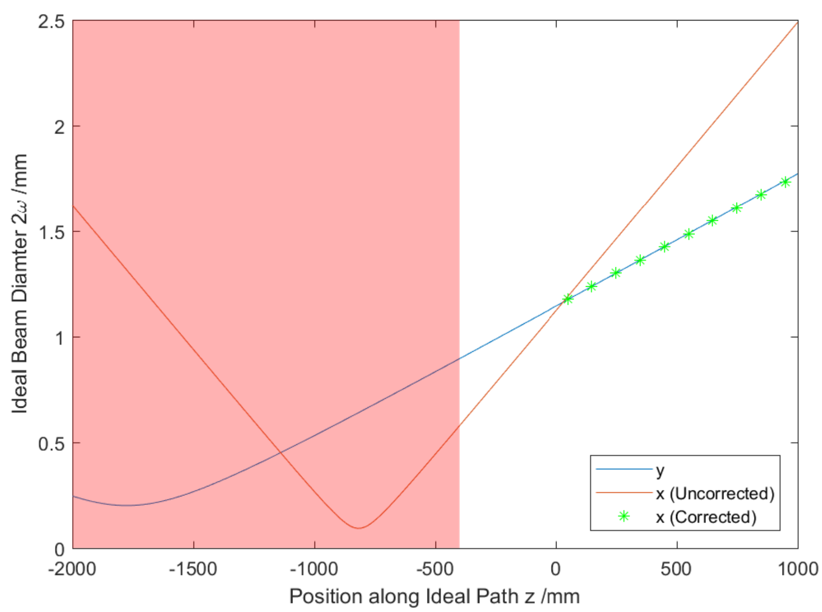

Figure 2.4: Plotted is the extrapolation of the two axes of the beam from the laser, showing clearly the astigmatism of the beam. The red region is inside the laser and therefore is unphysical. Also shown is the correction to the beam to bring both axes to the same size and divergence, giving an unastigmatic beam of the form give by equation 2.13.

Chapter 3

Beamsplitter

In this chapter I discuss how the single beam from the laser described in chapter 2, can be divided into multiple beams, one for each ion to be addressed, and subsequently be individually controlled. In section 3.1 I describe exactly what is needed at this stage of the beam to achieve what is required. In section 3.2 I look at possible ways of achieving this and why one was eventually chosen. Finally in section 3.3 I build and characterise a Free-Space beamsplitter.

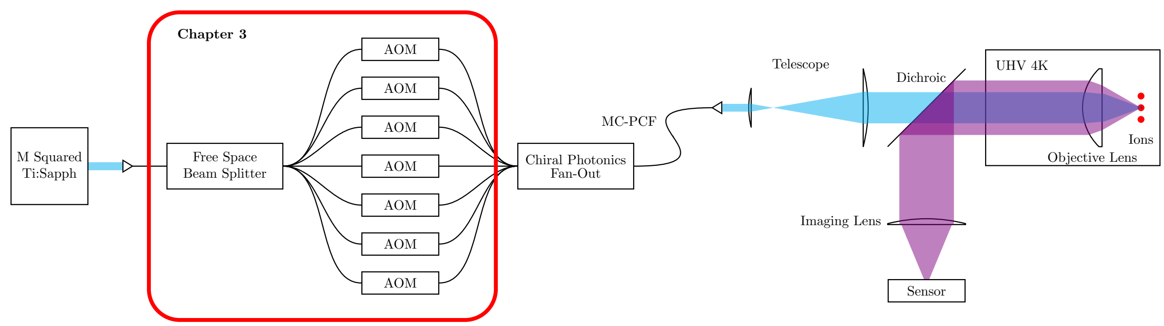

Figure 3.1: In Chapter 3 I choose a method to divide the beam into multiple channels.

3.1 Design Requirements

Eventually, we need to address a laser beam to each of a string of ions. Each beam must be spatially distinct, and must be independently controllable. In principle, we should like to address a string of 7 ions, meaning that at the initial beam must be divided into at least 7 equal parts.

Once separated, each beam can be controlled by an Acousto-Optic Modulator (AOM) [28]. For this purpose a fibre-coupled AOMs was acquired, being Brimrose TEM-110-10-110-400-2FP-HP. This choice of fibre-coupled AOM constrains the method of beamsplitting, because the beams after the splitting must be efficiently coupled into the necessary fibres. These were Nufern S405-XP, which have a core diameter of 3.0 µm, and a mode field diameter (MFD) of 3.3 µm at wavelengths of 400 nm. It has been decided since instead to use for the AOMs the S-M200-0.4C2A-3-F2S from Gooch&Housego, which provides the same constraint on the fibres used.

In general, the we would like the beams to the ions to contain as much power as possible. As such, any choice of beamsplitter must be made to minimise the optical loss. Things that we might therefore hope to avoid are repeated coupling into fibres and poor mode matching between fibres as well as generally minimising the number of components in the path of each beam where loss might be induced. Further, the beamsplitter must work at the power levels that might be typical in our experiments. In principle, we would want to make use of the entire power output of the laser, being around 2 W at 400 nm. As we see later in section 4.2, this limits the use of certain materials.

Finally, it would be hoped that the beamsplitting solution should be compact and self contained. This means having a well defined, relatively small size, and being able to be moved and reused if necessary.

3.2 Choosing a Beamsplitter

In splitting a beam, two broad choices present themselves. First, a beam can be split in-fibre, meaning that an optical fibre diverges into multiple fibres, and any light it contains is likewise partitioned. A second choice is to split a beam in freespace. This could be done by passing the beam through a series of optical beamsplitters, such a beamsplitter cubes, and then coupling each resulting beam into fibres.

3.2.1 Searching for an In-Fibre Splitter

An in-fibre splitter would have some advantages. It could be purchased as a complete product, would be compact and convenient to use, and wouldn't require maintenance after purchase. An eight-way fibre splitter could potentially be constructed from a series of connected two-way splitters, which are offered by many companies. However, we knew that some optical loss would occur at each stage, and we expected that a smaller loss might be achieved by a custom component that was designed for the intended division. Several companies were approached about this, the results of which I summarise here.

Schäfter+Kirchoff offer a two-way fibre-splitter, but when approached about a custom splitter, informed me that they couldn't extend this to wavelengths of 400 nm, or use directly the fibres from our AOMs. They offered a solution that they referred to a Fibre Port Cluster, which consisted of a series of waveplates and polarising beamsplitter cubes, being a freespace beamsplitter. They estimated the transmission through such a system to be 50 % to 60 %. Similarly, OZ Optics recommended a free space solution, using what they referred to as a Cascaded Plate Splitter. Since it was believed I could build such a system myself, these proposals were not taken further.

Fibersense&Signals told us that they were indeed able to build a fibre splitter for light at 400 nm, but were unable to do so with fibres of the requested core diameter of 3.0 µm. Matching the modes between a large fibre from the splitter and the small fibre to the AOMs would be a significant source of power loss, and so this was not considered a viable option. Fiber Optic Network Technology (FONT) informed us that the specific 'depressed clad' fibre used by the AOM was not suitable for use in a fibre splitter, but that they could use a multimode fibre of diameter of 50 µm, which would lead to losses, or instead use a different fibre of the desired diameter, but which would be doped with Germanium as opposed to being fused silica. We were warned that above 500 µW this fibre would exhibit losses due to photodarkening. As we see in section 4.5, these losses can be severe. Similarly, FibreBridge Photonics proposed a fibre splitter at the desired wavelength with the desired fibre diameter, with an estimated loss of 30 %, but warned us that further losses would occur due to photodarkening. They offered to send trial components to test for this, but it was decided to no longer pursue an in-fibre splitter solution, as the losses were expected to be significant.

3.2.2 Designing a Freespace Splitter

Having discovered that an in-fibre splitter would lead to large losses, the decision was made to build a freespace splitter. This would have certain advantages. First, it could be build relatively cheaply from widely available components, namely mirrors and beamsplitter cubes. It can also easily handle a wide range of wavelengths, and isn't limited by high input beam powers. It would however be larger, and require maintenance, as it might be expected that mirror alignments would drift over time.

There are two broad ways of doing this. First, the beam split by a series of polarising beamsplitter (PBS) cubes, with a half-waveplate between each cube controlling the polarisation. A schematic of such a beamsplitter is shown in figure 3.2. It would have the advantage of having the power in each output O1-7 being controllable using the waveplates. However, it would be relatively expensive to build, due to the need for many half-waveplates and PBSs. Coupling into the output fibres may also be inefficient do to the signficant path difference between the different outputs.

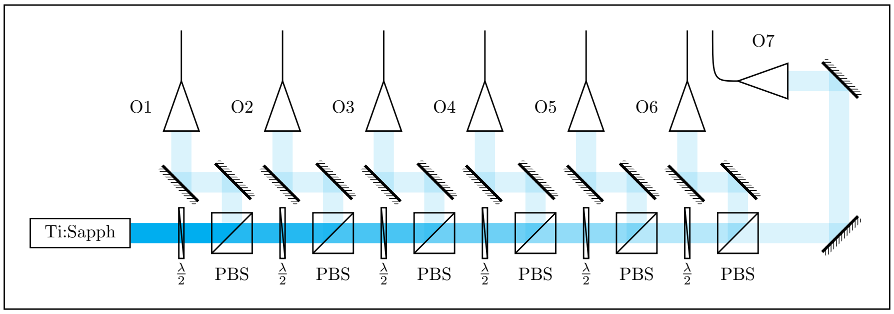

Figure 3.2: The beam can be split into seven equal beams using a set of 7 equal outputs, by sequentially splitting off a seventh of the beam using a half-waveplate and a PBS. Seven fibre collimation packages are then used to couple light into output fibres O1-7, with alignment provided by 2 mirrors per output.

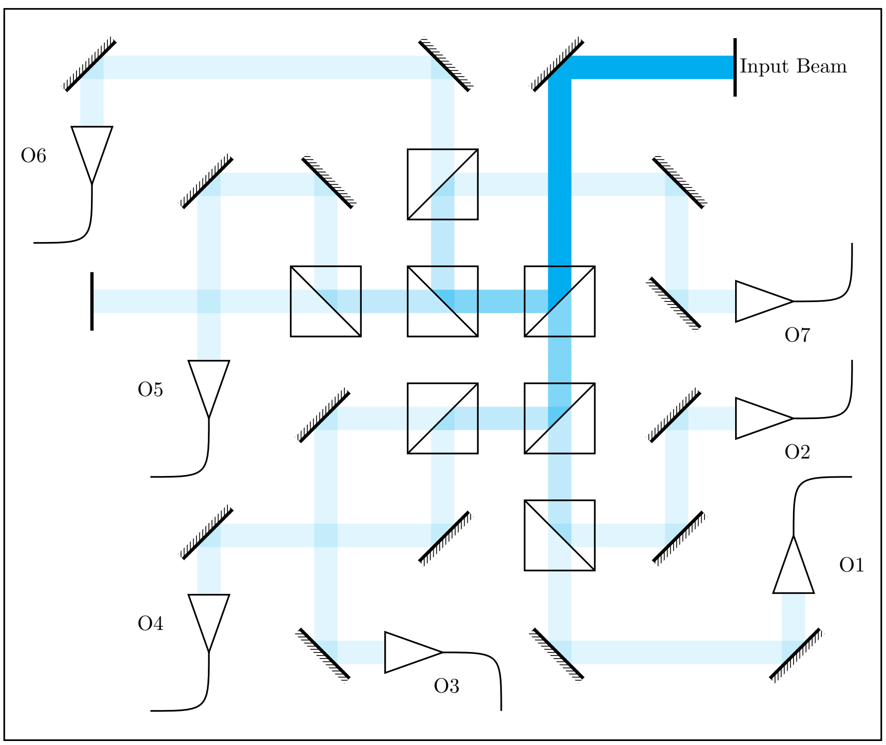

Figure 3.3: Depicted is the layout of the freespace beamsplitter I built. The beam is split in half 3 times by 7 BS cubes. The design is compact, with little unused space between components. Each beam fraction has a roughly equal path length, differing by at most a few centimetres, to make coupling into the output fibres easier. Space is left on the left of the diagram where future use might be made of the spare output beam, and space is left at the input beam for an additional mirror and lens, for example to bring the beam to the required height or for collimation.

The second way to build a beamsplitter in freespace is to dispense with polarisation optics and instead simply divide the beam into 8 using a series of 50-50 beamsplitter cubes (BS). This has the advantage of being cheaper and smaller, due to not required PBSs and half-waveplates. It means however that the power in each output cannot be controlled, and that necessarily the beam must be divided into 8 rather than 7, which may not matter if some further use can be found for the 8th output. I decided these downsides to be minor and so I built the beamsplitter depicted in figure 3.3. It consists of a cascade of 7 BS cubes, with each fraction of the beam passing through 3. Each fraction is then coupled into an output fibre through a fibre collimation package, with the beam position controlled by two mirrors.

3.3 Characterisation of the Beamsplitter

To make the freespace beamsplitter as compact as possible, miniature optical mounts were bought from the MNI range of Radiant Dyes. The whole assembly fit on a breadboard that was 250 mm × 300 mm in size, and was 80 mm in height. This somewhat larger than the proposed size of, for example, the FONT in-fibre solution, being 165 mm × 104 mm × 34 mm. Space was left near the eighth output for additional optics if use might be made of it in future. For the purposes of testing the splitter for losses, only a single mirror was placed on the breadboard prior to the first BS cube, with an additional, table-mounted mirror, not shown in figure 3.3 used to raise the beam to the height of the breadboard. The use of two mirrors at the input means that the coupling into each output fibre needs only be optimised once. If subsequently, the input beam were to change position, the use of two mirrors at the input could in principle align all outputs simultaneously.

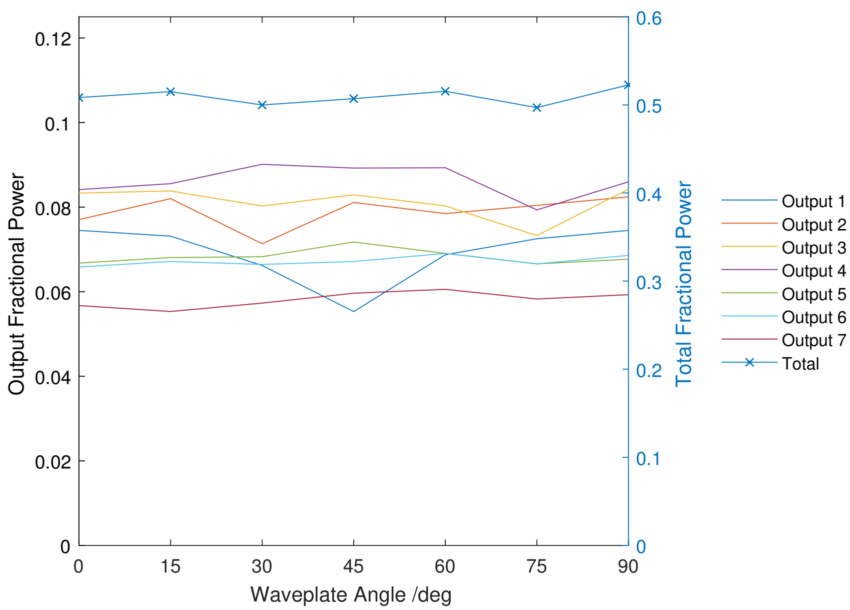

Figure 3.4: Plotted are the optical powers at the outputs of the beamsplitter, and the total output power, as a fraction of the input power. Measurements were taken across a range of polarisations, in the hope of reducing power loss. Polarisation was controlled by rotating a half-waveplate, where angles of 0° and 90° correspond to the horizontal polarisation of the beam from the laser, and 45° to vertical.

I used a power metre to measure the total loss in power in the splitter. This was found to be approximately 50 %, with each output containing 7(1) % of the input power. This compares reasonably well with the proposed freespace splitter proposed by Schäfter+Kirchoff. It was however still higher than the loss I had expected. The BS cubes were Thorlabs BS010, which had a stated maximum loss of 10 %, giving an expected power in each output of 9.1 % of the input power. It was suggested to me that I measure the losses over a range of polarisations. I did this by placing a half-waveplate in the input beam using it to rotate the polarisation of the beam. The fractional power as a fraction at each output is shown in figure 3.4. We see no significant reduction in power loss with changes in polarisation. Although by design, all reflections were through 90°, spatial constraints on the breadboard meant that this was not always true in practice, or that some surfaces became dirty due to the difficulties of assembling the splitter by hand. This may account for some further loss.

Chapter 4

Using the Multicore Photonic Crystal Fiber

In this chapter I discuss the properties and use of a Multicore Photonic Crystal fibre (MC-PCF) that we acquired. Its broad function was to carry the ion addressing beams from the laser and beam splitter described in previous sections, to the lenses described in the next section that focus the beams onto their respective ions. I begin by discussing briefly the nature of photonic crystal fibres in section 4.1, providing some results that I will use subsequently. In section 4.2 I discuss a notable loss mechanism in optical media, photodarkening, where optical loss can vary strongly with time and intensity, that motivates tests I did later. Next I describe in section 4.3 the fibre we acquired and characterise certain properties of it. Finally in sections 4.4-4.6 I discuss a product we purchased that couples light from several individual fibres into the MC-PCF, and tests I did that informed the manufacturing of this device.

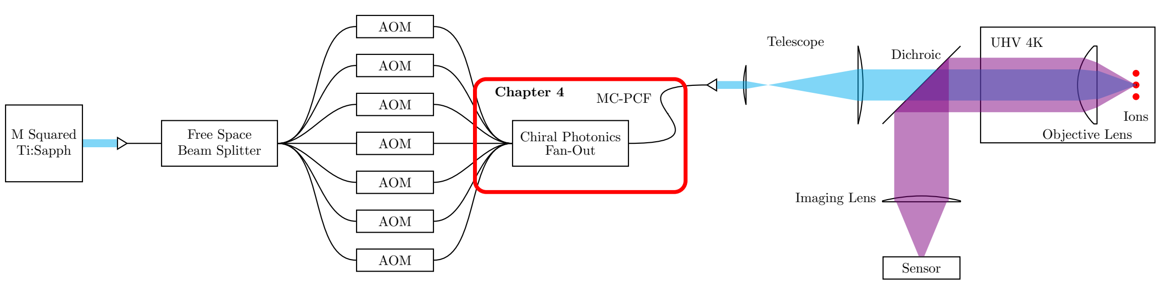

Figure 4.1: In Chapter 4 I discuss the MC-PCF and how I coupled light into it.

4.1 Photonic Crystal fibres

The transmission of light through optical waveguides in the form of silica fibres is well established [27]. In give here a brief overview of the salient features of optical fibres.

A typical optical fibre might consist of a thin cylindrical core with radius a made of some kind of material, with constant refractive index n_1, surrounded by some cladding material with index $n_2 < n_1$. Light repeatedly reflects off the core-cladding boundary and so is transmitted along the fibre. Such a Step-Index fibre can be characterised by a numerical aperture

$$\mathrm{NA} = n \sin \theta_{\max} = n^{-1} \sqrt{n_1^2 - n_2^2} \tag{4.1}$$

where n is the refractive index of the surrounding material, typically air, and θ_{max} is the greatest angle allowed between an incident beam and the axis of the fibre that would ensure total internal reflection at the core-cladding boundary.

For such a fibre carrying light of wavelength λ, a further characteristic V number can be defined.

$$V = \frac{2\pi}{\lambda} a\mathrm{NA} = \frac{2\pi}{\lambda n} a\sqrt{n_1^2 - n_2^2} \tag{4.2}$$

In general, light propagates in a waveguide in different optical modes. This V number characterises the number of modes that can be transmitted in the fibre [29]. Below $V \approx 2.4$ the fibre guides only a single optical mode, the Gaussian mode approximating equation 2.13, and for large V the number of guided modes from equation 2.11 is

$$N_{\mathrm{modes}} \approx \frac{1}{2} V^2 \tag{4.3}$$

For a step index fibre, the mode radius ω, defined as the radial position where the electric field drops to e^{-2} of it maximum value, of the fundamental, approximately Gaussian, mode is given by [30]

$$\omega = a\left(0.65 + \frac{1.619}{V^{\frac{3}{2}}} + \frac{2.879}{V^6}\right) \tag{4.4}$$

Here we note that in the limit of $V^{\frac{3}{2}} \gg 1.619$, the mode size is only weakly dependent on the V number and is mostly a function of the core radius a. For example, the fractional variation in ω is less than 5 % for values of $V > 15$

Photonic Crystal fibres (PCFs) are a special form of fibre which possess substructure on the micrometre scale [31, 32]. Rather than consisting of several materials of different refractive indices, a typical PCF is a fibre of one material, but with an regular array of air holes runnning through it, with the central air hole missing. This structure can be considered analogous to a Step-Index fibre, with the central, hole-free region being the core, and the surrounding photonic crystal being the cladding. For such a fibre, the numerical aperture can now be taken to define an effective refractive index n_{eff} for the photonic crystal structure.

$$V_{\mathrm{eff}} = \frac{2\pi}{\lambda} a\sqrt{n_{\mathrm{core}}^2 - n_{\mathrm{eff}}^2} \tag{4.5}$$

The value of n_{eff} can be tailored by varying the sizes of the holes and the distances between them, and in general $n_{\mathrm{eff}} = n_{\mathrm{eff}}(\lambda)$ is strongly dependent on the wavelength of light in use. This tunability can give PCFs many of their useful properties, for example, fibres can have very large NA [33], or a single fibre can be made to be single mode over a wide range of wavelengths [34].

The effective refractive index of a PCF can in general be found computationally [35] but it is instructive to examine certain limiting cases that might be of interest. Firstly, in the case that the wavelength is long comparing to the hole spacing and hole diameter. In this limit, the optical mode in the PCF may be significantly larger than the central core, and is distributed indiscriminately between the solid fibre and the air spaces. In this way, the effective refractive index can be approximated by averaging over the refractive indices of the solid and air regions of the fibre [36]

$$n_{\mathrm{eff}}^2 = (1-f)n_{\mathrm{core}}^2 + f n_{\mathrm{air}}^2 \tag{4.6}$$

$$V_{\mathrm{eff}} = \frac{2\pi}{\lambda} a f^{\frac{1}{2}} \sqrt{n_{\mathrm{core}}^2 - n_{\mathrm{air}}^2} \tag{4.7}$$

where f is the fraction of the fibre cross-section that contains air.

Another interesting case is where the wavelength is small compared to the scale of the structure. In this case, the light is confined primarily to the solid, central core. Further, if the air space fraction is very large, the central core can be modelled a solid, simple fibre, surrounded primarily by air, supported only by thin slabs of material. Such a model is given and tested in [37] and [38]. For such a fibre, the effective index and V number due to the slabs is given by

$$n_{\text{eff}} = n_{\text{core}} \left(1 - \frac{1}{8}\left(\frac{\lambda}{n_{\text{core}} t}\right)^2\right) \tag{4.8}$$

$$V = \frac{\pi a}{t} \tag{4.9}$$

where t is the thickness of the supporting slabs and a the radius of the solid core. In such a model, where the supporting slabs are thin compared to the size of the core $a \gg t$, the guided modes are contained primarily within the core, with the field amplitude inside the slabs decaying exponentially with the distance l into the slab as

$$\psi \propto e^{\frac{-\pi}{t} l} \tag{4.10}$$

Accordingly, this model of a solid, air-surrounded core supported by thin slabs may be appropriate when slabs separating solid regions are much longer than they are thick.

4.2 Photodarkening

Photodarkening is a process exhibited by many optical media, notably in silica fibres that have been doped with other elements [39, 40, 41]. It is a process by which the optical absorbance of a material changes over time in response to exposure to light. It could present a significant obstacle to our hope to perform single ion addressing, as for the faithful performance of quantum gates, an ion must be exposed to a well known electric field intensity, and a high intensity if these gates are to be performed quickly. If the addressing setup were to introduce time varying and significant losses, this would not be possible. In this section I describe the mechanisms that lead to photodarkening in Germanium-doped silica fibres and describe a simple model that reproduces some of the salient features, in order to motivate the tests I do in section 4.5.

Colour centres are defects in the crystal structure of doped silica. They can scatter light that is incident upon them and so their presence increases optical losses. The formation of colour centres can itself be driven by exposure to light, and so the optical power lost in a material increases over time with exposed to light at certain wavelengths. In Ge-doped silica, this proceeds as follows. In its initial, state, the material will have some number of Ge−Si or Ge−Ge bonds. This bond is broken by a two-photon absorption process [42], $\mathrm{Ge{-}Si} \xrightleftharpoons{2\hbar\omega} \mathrm{Ge^{\bullet}{-}Si^{+}} + \mathrm{e^{-}_{free}}$, exciting an electron to pathways formed by interconnected Ge centres. The electron may then react with another Ge atom to form a colour center Ge(1) or Ge(2). These colour centres may spontaneously release the electron again due to thermal excitation, or my be induced to do so via a single photon. A model of the evolution of the various electron populations is given in [43]. A simple model of the evolution of the population n of a single type of colour centre, when a sample is exposed to a time constant intensity of light, is

$$\frac{dn}{dt} = \Gamma_f (N - n) - \Gamma_r n \tag{4.11}$$

where N is the total population of electrons available for colour centre formation, which I assume to be constant, Γ_f is the rate of electrons falling into a colour centre, and Γ_r is the rate of trapped electrons being released from the colour centre. In the case of the sample initially being free of colour centres, $n(t = 0) = 0$, equation 4.11 is solved by

$$n(t) = \frac{\Gamma_f}{\Gamma_f + \Gamma_r} N \left(1 - e^{-(\Gamma_f + \Gamma_r)t}\right) \tag{4.12}$$

So we see that after a long time, the colour centre population reaches a steady state, where the rate of colour centre formation is exactly counterbalanced by the rate of colour centre release. To first order in n, the probability of a photon being absorbed by a colour centre is proportional to n [44] and so we would expect the power transmitted T by a doped silica fibre exhibiting photodarkening when exposed to a constant intensity of light to decrease as

$$T(t) = T_\infty + (T_0 - T_\infty)e^{-t/\tau} \tag{4.13}$$

where T_0 and T_∞ are the initial and final transmission respectively and $\tau = (\Gamma_f + \Gamma_r)^{-1}$ is the time for the transmitted power to fall $\frac{1}{e}$ towards its steady state value.

Of course this model hides the other other dependences of the colour centre population evolution. The rate Γ_r contains both the induced release of an electron by a photon, which depends linearly on the intensity, and the thermal release, which scales exponentially with temperature. Likewise the rate Γ_f depends on the rate of Ge−Si being broken, which occurs by a two-photon mechanism and so depends on the square of the intensity.

4.3 Characterising the MC-PCF

A photonic crystal fibre was provided by Michael Frosz at the Max Planck Institute for Light. Figure 4.2 shows an SEM micrograph of a cross section through this fibre. The fibre contains an array of solid cores separated by pockets of air, depicted as light and dark regions respectively. Our hope was to use each of these solid cores as a separate optical waveguide, and so the fibre would constitute a Multi-Core Photonic Crystal fibre (MC-PCF).

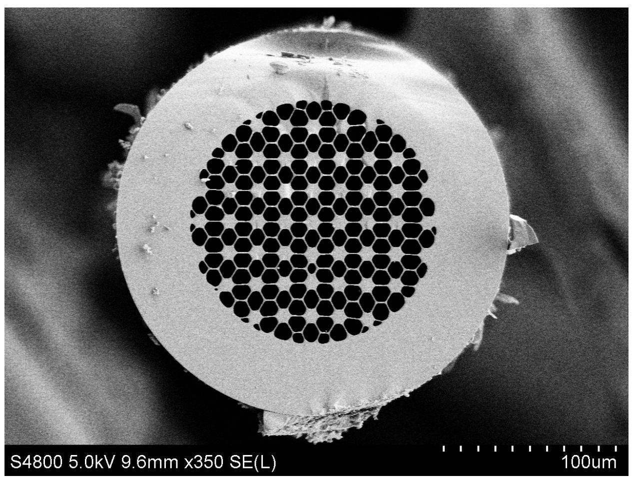

Figure 4.2: Micrograph of the cross section of the PC-MCF showing an array of potential cores. Solid silica cores appear as light regions, separated by dark, air-filled regions. Image courtesy of Michael Frosz

The core centres are spaced at 16 µm along the short axis of the array and 18.5 µm along the long axis, depicted in figure 4.2 as horizontal and vertical respectively. On the central row, the error in the vertical position of the centre of each core, is at most 18.5 µm. Each core has a diameter of $a = 8.5$ µm. The thin regions joining the cores along the central horizontal row are $t = 0.6$ µm thick at their centres with this thinnest region being at least 5 µm long. Thus we might be justified in modelling the cores according to the model given in section 4.1 of solid, air-spaced cores supported by thin slabs.

An estimate of the V number of these cores can therefore be given by equation 4.9 as $V = 22$ and therefore the fundamental mode radius is given by equation 4.4 as $\omega = 2.8$ µm, or equivalently the mode field diameter is MFD $= 2\omega = 5.6$ µm

The use of the MC-PCF in this manner can be seen in figure 4.3. It shows images of one end face of the MC-PCF, projected via a lens onto a piece of paper, which I photographed with a camera. Figure 4.3a shows the image when I shone a wide laser beam onto the entirety of the other end of the MC-PCF, thus coupling light into all the cores of the fibre. I rotated the fibre to make the correspondence with figure 4.2 more apparent. To produce figures 4.3b-4.3h, I focused the laser light so that it illuminated approximately one core and used a translation stage to move the fibre so that the beam coupled into a row of cores in turn.

Of course these images betray the difficulty of dealing with the MC-PCF, showing damage to the ends of some of the cores at the top of figure 4.3a and showing some light tranmission through cores adjacent to the intended core in, for example, figure 4.3c. To be able to more precisely measure the beam leaving the MC-PCF, I pointed it into the sensor of a Beam Profiler and used it to estimate the radius of the beam

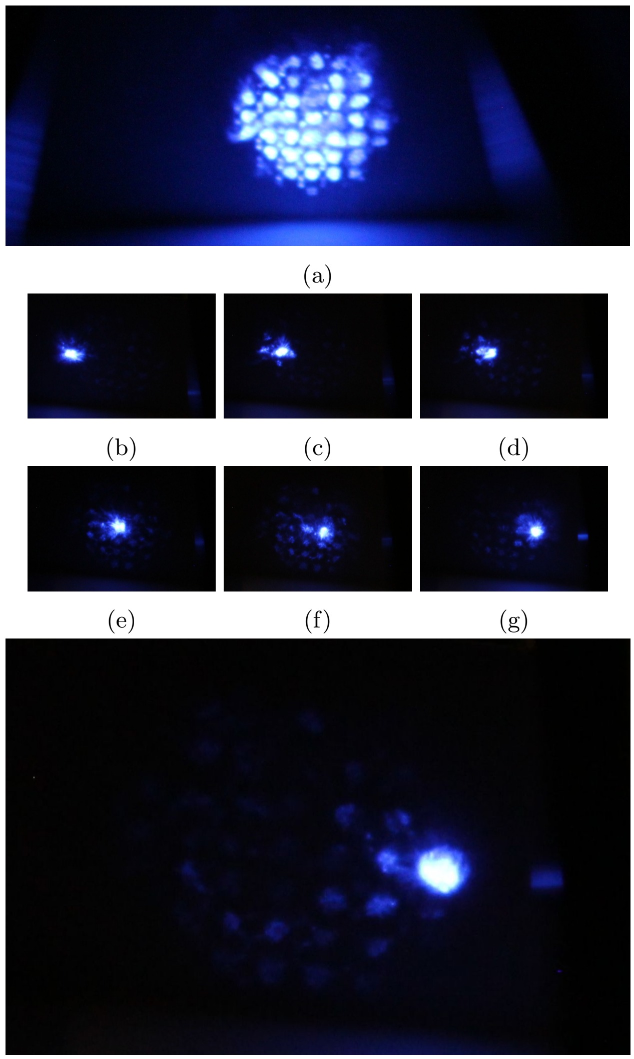

(a)

(b) (c) (d)

(e) (f) (g)

(h)

Figure 4.3: Figure 4.3a shows an image, projected onto a piece of paper, of the face of the MC-PCF with light coupled into all the cores, giving a similar appearance to figure 4.2. Visible is that certain core are damaged and therefore appear dark, which in later sections will become a problem. Figures 4.3b-4.3h the same thing but with light coupled into approximately one of the central row of cores. It can be seen that some light also couples into adjacent cores, either due to bad in-coupling, or crosstalk with in the MC-PCF

along two axes at 4 points along the propagation axis of the beam for several different cores of the MC-PCF. Figure 4.4 shows an example of this for the central core. Figures 4.4a and 4.4b show the intensity profile of the beam along two axes at the 4 different positions. They show an approximately Gaussian shape, as expected given equation 2.14, which grows with distance.

I fitted each of these profiles to a Gaussian curve and used this to estimate the radius of the beam at each position. Figure 4.5 shows the change in beam size along each axis for 5 different cores. As expected from equation 2.15, in the far field regime, many Rayleigh Lengths from the face of the MC-PCF, the beam size can be seen to increase approximately linearly with distance. The starting beam size appears to differ for each line. This is because the distance between the MC-PCF and the beam profiler differs slightly for each measurement as the MC-PCF moves while I re-coupled light into different cores.

Using this data I estimated the divergence angles of the beam leaving the MC-PCF to be

$$\theta = 4.8(9)^{\circ} \tag{4.14}$$

This value will be used later on when designing and simulating the beam for single ion addressing. Using the earlier estimate of the fundamental mode radius of cores of the MC-PCF of 2.8 µm I likewise estimated from equation 2.17 a value of M^2 to be

$$M^2 = 1.8(3) \tag{4.15}$$

4.4 Coupling Fibres into the MC-PCF

For the measurements described so far, I have coupled light into the cores of the MC-PCF with some difficulty, by manually aligning the mode from the laser with the mode of the cores using mirrors, lenses and translation stages. This has several obvious disadvantages. Firstly, we desire that the setup be compact, self-contained and movable. Secondly, it is difficult to reliably couple efficiently into the fundamental mode of just one core at a time. Finally, it is difficult to expand this setup to allow coupling of separate beams into different cores simultaneously, which we require if we are to image each core onto its own ion and to manipulate them independently.

For these reasons, we hoped to couple the fibres coming from the AOMs directly into the MC-PCF. Such systems have been built for many cores using mirrors and lenses such as in [45], but they are difficult to build, maintain and to scale up. We would prefer a device that could directly fuse input fibres into the cores of the MC-PCF. For our purposes a device, a fan-out, would take up to 7 input fibres, the pigtails, and would need to both match the mode sizes between these fibres and the cores of the MC-PCF, and reduce the pitch between them to match the core spacing of the MC-PCF. We found a company, Chiral Photonics, that was able to produce such a fan-out that they could customise for the MC-PCF, which we would provide to them, at the desired wavelength of 400nm.

They informed us that for their production and characterisation, they needed to construct a fan-out on both ends of the MC-PCF. Since we needed only one fan-out, and a bare end of the MC-PCF, we asked them if one end could be designed for 400 nm, as desired, and the other for 729 nm. We could then cleave the MC-PCF in the middle, giving us what we needed, and also a component that could be used in future experiments. They agreed this was possible, advising us that could build both fan-outs with fibres designed for 630 nm, and then splice these fibres at one end to 405 nm fibres. Figure 4.6 shows this schematically.

Working at 400 nm and in principle at powers around ∼100 mW we were concerned that photodarkening would occur if the optical path contained doped sections. Chiral Photonics told us that they were able to use pure silica fibres for the pigtails, but that their Vanishing Core and pitch reduction techniques [46, 47] required materials with well chosen refractive indices to ensure optimal mode matching between fibres, and so it was unavoidable that a short section of germanium doped silica would be present in the device. Of course this could drastically reduce the light intensity that would eventually reach the ion trap and so is undesirable. In an effort to resolve this, we arranged for Chiral Photonics to produce a set of possible components for testing. This would not couple into the MC-PCF but rather would just couple between two single mode fibres via one of their vanishing core structures. We would then expose these structures to light at powers and durations comparable to those that they would experience in a real experiment, and monitor

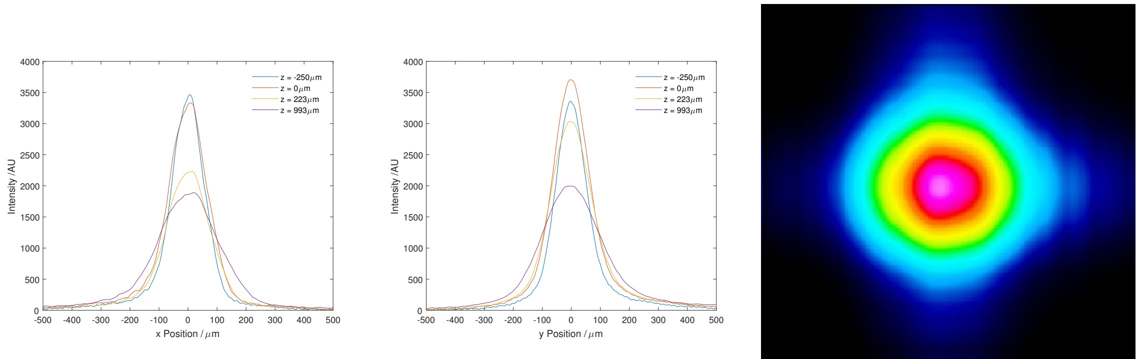

(a) (b) (c)

Figure 4.4: Figures 4.4a and 4.4b show cross-sections, on the x and y axes respectively, of the power intensity of a beam coming from a core of the MC-PCF at 4 positions along the beam. Figure 4.4c shows a colour intensity plot of the same beam at $z = 0\,\mathrm{mm}$, showing qualitatively the approximately Gaussian shape of the beam. The z positions of the 4 measurement positions is are given according to the convention of the beam profiler and the curves are all centred on the origin for clarity. The origin of the z axis follows the convention used by the beam profiler.

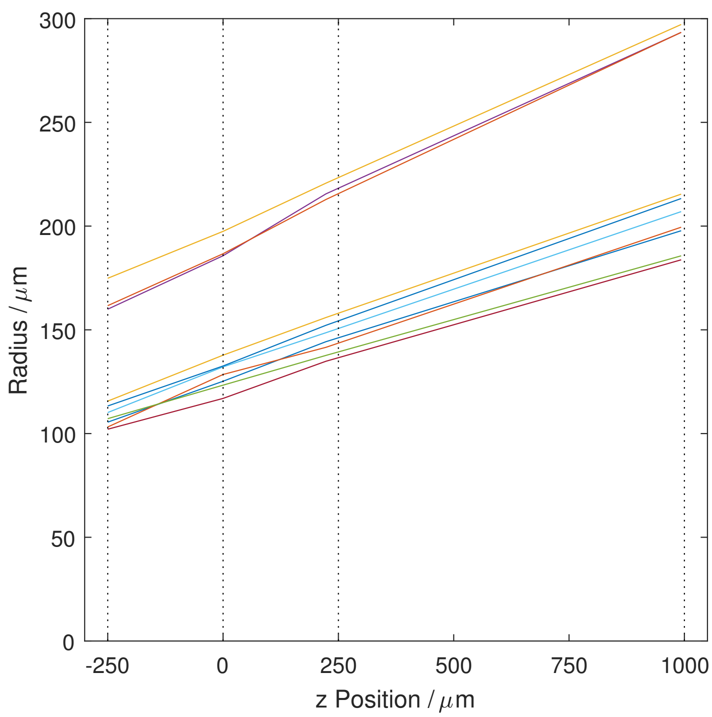

Figure 4.5: Plotted are estimates of the growth in beam radius of various cores of the MC-PCF at the four Beam Profiler positions, approximately showing the far field beam divergence angle. Each coloured line traces the evolution either the horizontal or vertical radius of the beam from a different core of the MC-PCF, as measured at the four measurement positions inside the Beam Profiler. These measurement positions are shown by vertical dotted lines.

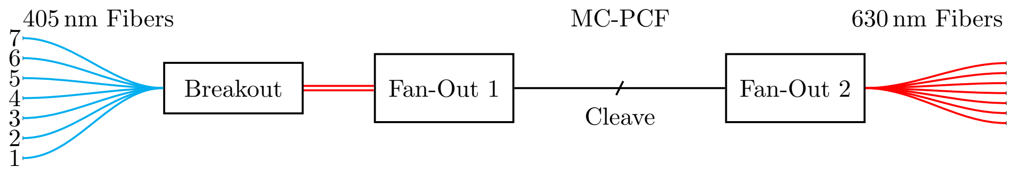

Figure 4.6: The components of the proposed Chiral Photonics product. The MC-PCF has a fan-out on both end to 630 nm fibres. One end is then spliced to 405 nm fibres in the Breakout box.

the change in power transmitted through the component over time. These results would then inform the design of the fan-out.

4.5 Testing for Photodarkening

We received 4 structures to test, structures I-IV, and 3 copies of each. My setup was to measure the total power transmitted through the test structures over time. To ensure that all any measured change in transmitted power was due to darkening in the test structure, and knowing that the laser power was liable to drift slightly over time, or that the laser may be disturbed and briefly fall out of lock, I used a pickoff mirror to monitor the power supplied to the structure. I was also aware that the mirrors I used to couple into the input fibres may move slightly over time. This would be difficult to correct for in real time, but I attempted to ensure that the effect would be small by efficiently coupling into the fibre before starting measurements, and then realigning after measurements were completed. If a large increase in transmitted power could be achieved solely by realigning mirrors, it was a sign that the measured decrease in power could not reliably be attributed to photodarkening in the test structure.

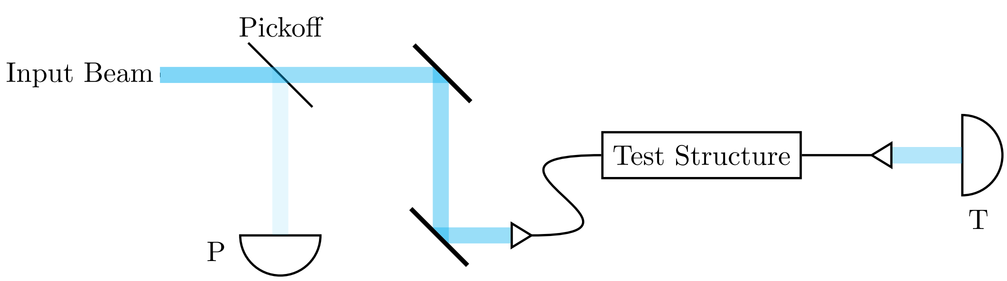

Figure 4.7: Setup used to measure photodarkening in the test structures. Represented by semi-circles are power meters, measured pickoff power P and transmitted power T. To control for fluctuations in laser power, the ratio $\frac{T}{P}$ is plotted in figures 4.8 and 4.9.

Hoping to simulate the effect of long term exposure to light at 400 nm, I ran a preliminary test on structure I, passing 600 mW, much more than intended for normal operations, through it. The results were not promising, as the power transmitted dropped by 80 % even in the short time that it took me to set up the measurements. Thus I next decided to perform longer tests at 100mW. I tested structure II at this power, having been told by Chiral Photonics that they expected it to perform best. Figure 4.8 shows the results of this test, the decay in transmitted power over 6 hours. Visible are 2 spikes, which correspond to sudden and temporary fluctuations caused by the laser being disturbed, probably by nearby movement in the room.

Clearly these results are still troubling. Over 6 hours, the transmitted power decreased by 57 %. This likely means that future experiments will have their power limited severely compared to what was initially

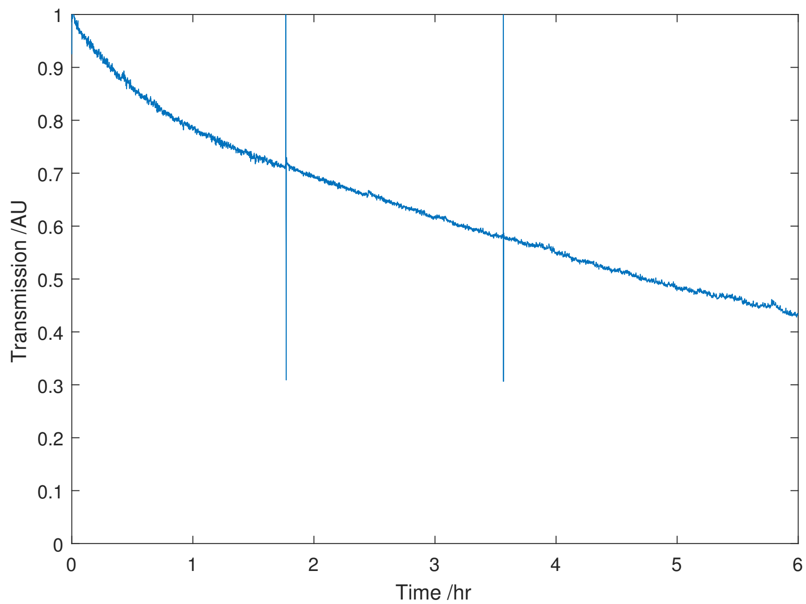

Figure 4.8: The decay of the power transmitted through structure II over 6 hours when the structure was exposed to 100mW total power. Plotted is the ratio between the measured transmitted power and the power measured at the pickoff, normalised relative to the initial value. Visible are two spikes caused by the laser relocking after being disturbed, for example by external vibrations.

Structure	Steady State Tranmsission T_∞ /AU	Decay Time τ /h
I	0.13	3.9
II	0.79	21.6
III	0.43	1.8
IV	0.79	5.7

Table 4.1: Tabulated are the values of the decays constants of the changes in transmission of the various components shown in figure 4.9, with values fitted to equation 4.13. Structures II and IV show comparable total loss, but structure II over a much longer timescale. Structure II was thus chosen for the final Fan-Out.

hoped. In line with the simple model given in section 4.2, fitting this data to an exponential decay of the form given in equation 4.13 suggests that the power transmitted will tend to around 29 mW with a $\frac{1}{e}$ time of 4.2 h. To try to avoid photodarkening I therefore decided to limit the power used in my tests to less than this and tests on the remaining components were performed at 20 mW.

Figure 4.9 shows the transmission change over time for the 4 structures types when exposed to 20 mW at 400 nm. The measured or projected steady state transmission and characteristic decay times of the four structures are summarised in table 4.1.

Clearly this data is somewhat imperfect. Structures I and III show oscillations of a few percent in the transmitted power. This is likely due to some oscillation in the input fibre coupling, for example the mirrors moving back and forth slightly, as the power measurements at the pickoff did not show a comparable change. However, I achieved no significant improvement in coupling after finishing measurements, so the large decrease in power is enough to draw a negative conclusion. The data for structure III shows step changes in the transmitted power. This is due to the laser being disturbed during the measurements causing the laser to unlock and relock. This caused a change in the power emitted, as recorded in the pickoff measurements, and a change in the mode size and hence coupling efficiency, giving a simultaneous but different change in the measured transmitted power.

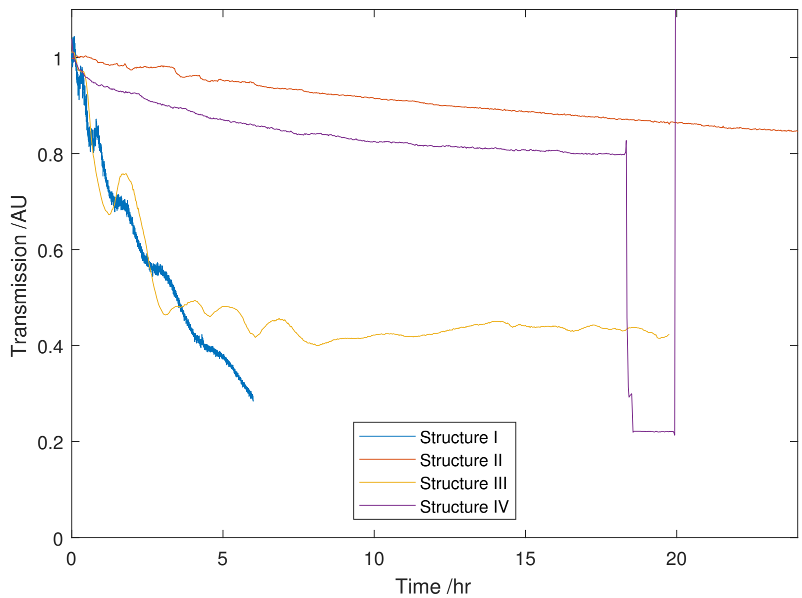

Figure 4.9: Plotted is the measured power transmitted through the 4 structures when exposed to 20 mW over time, divided by the power measured at the pickoff, normalised relative to the initial value.

4.6 The Final Product

Given these results, it was decided in consultation with Chiral Photonics that structure II was the least susceptible to photodarkening. We sent them the MC-PCF as agreed and recieved it back with the fan-outs attached and cleaved the MC-PCF to leave just the 400 nm half, as seen in figure 4.10.

Chiral Photonics had intended to measure the crosstalk as well, but due to their accidental breakage of the MC-PCF, they were unable to do so. Nevertheless I wanted to measure the crosstalk between the different channels, that is, the amount of power contained in the different cores of the MC-PCF when light is input into only of the fibres of the fan-out. To this end, I connectorised input fibre 3, coupled light into it and then produced an image similar to 4.3. I moved an iris across the image, blocking all spots except one at a time, and measured the power. The results are summarised in table 4.2.

These results are promising. The largest crosstalk is 4.6×10^{-3}. Ideally we should like the crosstalk to be of the order of 1×10^{-4}[20]. It is possible that the Fan-Out we acquired does not align the input fibres perfectly with the cores of the MC-PCF, leading to light being coupled into multiple cores directly, similar to when I coupled light into the MC-PCF manually. If we are confident that the Fan-Out itself does not introduce significant cross talk, we might expect that the crosstalk is due to the small amount of the mode in each core that spreads along the thin regions of silica that connect the cores. For small levels of crosstalk, this is effect is expected to increase linearly with the length of the MC-PCF. Since this is approximately 1 m long, there is plenty of scope to reduce crosstalk further. Additional crosstalk might be due to damage to the MC-PCF, or the effect on the mode of the imperfect endface of the MC-PCF. These are harder to quantify, but might also be reduced in future.

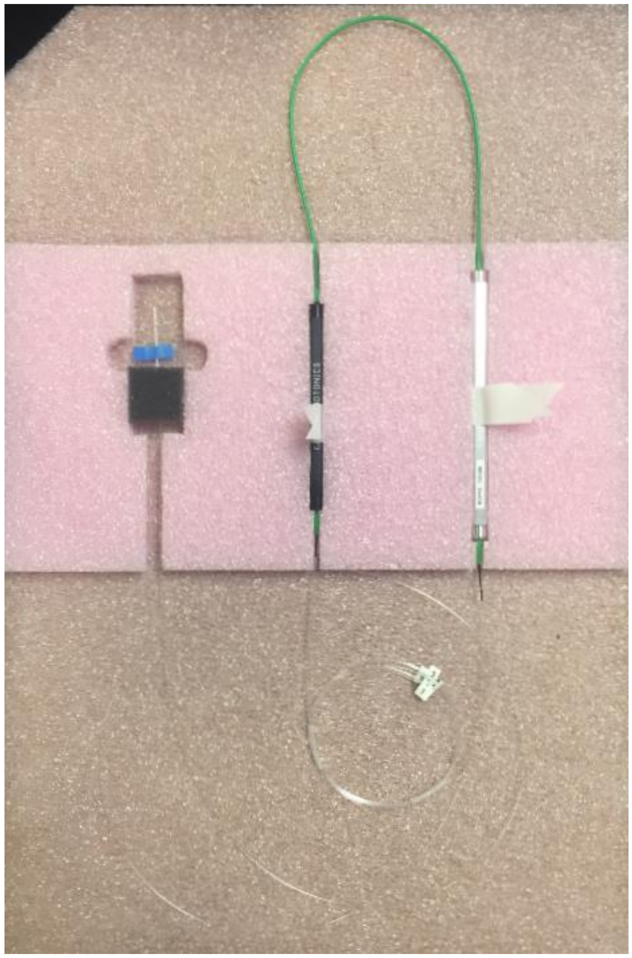

Figure 4.10: A photo of the Fan-Out purchased from Chiral Photonics to couple light into the MC-PCF. Centre-left is the protected endface of the MC-PCF, centre is the Breakout, and centre-right the Fan-out, as described in figure 4.6. At the bottom is coiled up the MC-PCF

Core	Power /µW	Fractional Power
1	3.5	1.2×10^{-3}
2	13.4	4.6×10^{-3}
3	2910	1
4	8.6	3.0×10^{-3}
5	3.7	1.3×10^{-3}
6	2.7	9.3×10^{-4}
7	2.0	6.9×10^{-4}

Table 4.2: Tabulated are the measured powers contained in the output beams of the cores of the MC-PCF when only core 3 receives an input from the Fan-Out. We see that this crosstalk is largest in the cores adjacent to the intended core 3, but is everywhere small as a fraction of the power in core 3.

Chapter 5

Single Ion Adddressing

In this chapter I discuss the system I designed in order to focus the row of beams at the endface of the Multicore Photonic Crystal Fibre described in chapter 4 onto a string of ions. This was achieved by a sequence of four lenses. I also discuss briefly the use of the same lenses to image the ions for the purpose of qubit measurement, which is achieved by a dichroic mirror. In section 5.1 I discuss some optical effects that are relevant to the work I do later in order to motivate decisions I made. In section 5.2 I describe the goals that I sought to achieve by the choice of lenses I made, and some of the physical and theoretical constraints that limited these choices. I then describe in section 5.3 the simulation of the beams under the action of these lenses, showing the potential for successful single ion addressing. Finally in sections 5.4 and 5.5 I build my designed system, attempt to characterise it and then to explain why it didn't perform as expected.

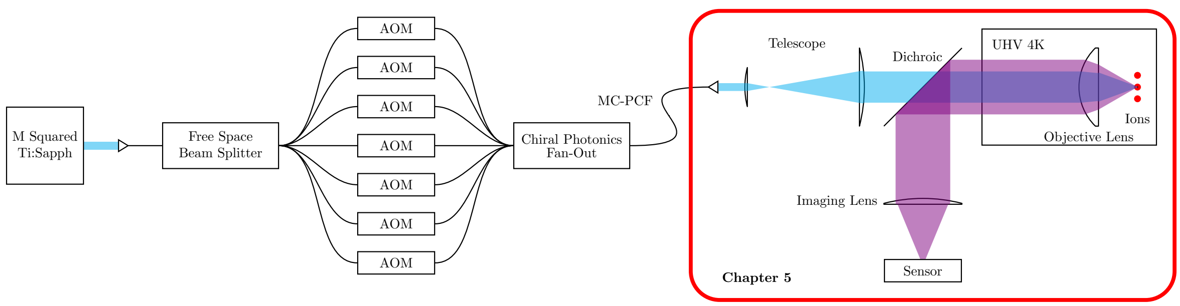

Figure 5.1: In Chapter 5 I discuss focusing each beam to a single ion, and how I simulated and then characterised the system.

5.1 Optical Effects and Aberrations

In designing a system of lenses, I expect to encounter various optical phenomena, where the simulated action of a system of physical lenses differs from that of a system of idealised lenses. Such aberrations can limit the minimum achievable spot size at the focal point, limit our ability to distinguish between nearby objects, and generally distort any image produced by an optical system. In order to inform and motivate work I do in later sections, in this section I present some aberrations, the limits they impose, and how to avoid them. The results I present are specific to the project that follows, and a more rigorous treatment of aberrations can be found for example in [48].

5.1.1 Edge Effects in Lenses of Finite Size

A notable difference between a real lens and a ideal lens is that any real lens must have a finite radius. Any light passing through such a lens will therefore in general experience refraction. This limits the minimum achievable spot size to which a beam can be focused. For example, an infinite plane wave passing through an infinite lens will be focused to a perfect spot, whereas plane waves incident on a finite circular aperture will produce an Airy disk [48]. The Abbe diffraction limit for the spot diameter d of such a scenario is

$$d = \frac{\lambda}{2\sin\theta} \tag{5.1}$$

for light for wavelength λ where θ is the half angle of the cone defined by the focal point and the edge of the lens. Gaussian beams passing through a finite lens show a similar phenomena. For a collimated Gaussian beam with a radius ω much smaller than the radius of a lens with focal length f, the focused beam has its waist at the focal point of the lens, with a minimum spot size ω_0 of

$$\omega_0 = \frac{f\lambda}{\pi\omega} \tag{5.2}$$

Thus a larger collimated beam is focused to a smaller spot. However, this is limited by diffraction from the edge of the lens. Figure 5.2 shows a simulated cross section through the focal point of a Gaussian beam at its waist after being focused by a lens with effective focal length $f = 25\,\text{mm}$ and a radius $a = 12.5\,\text{mm}$. This was done for a variety of different initial beam sizes ω. It can be seen that for small ω, the beam approximates a Gaussian spot, with the spot size ω_0 decreasing, and the peak intensity increasing, as ω increases. At larger $\omega > 4\,\text{mm}$ however, the beam diverges from a Gaussian beam, and appears more like an Airy function, with side peaks adjacent to the main peak, broadening the overall intensity distribution, and decreasing the peak intensity. A reasonable guide therefore is that to achieve the best possible focused spot of a Gaussian beam by a lens, the ratio between lens radius and beam radius should be around $\frac{a}{\omega} \approx 4$. Less that this sees a smaller spot size, greater than this means larger side lobes. This limit is where diffraction starts to become important, and corresponds to an electric field amplitude at the end of the lens of $e^{-4} \approx 2\,\%$ of the peak amplitude at the centre of the lens.

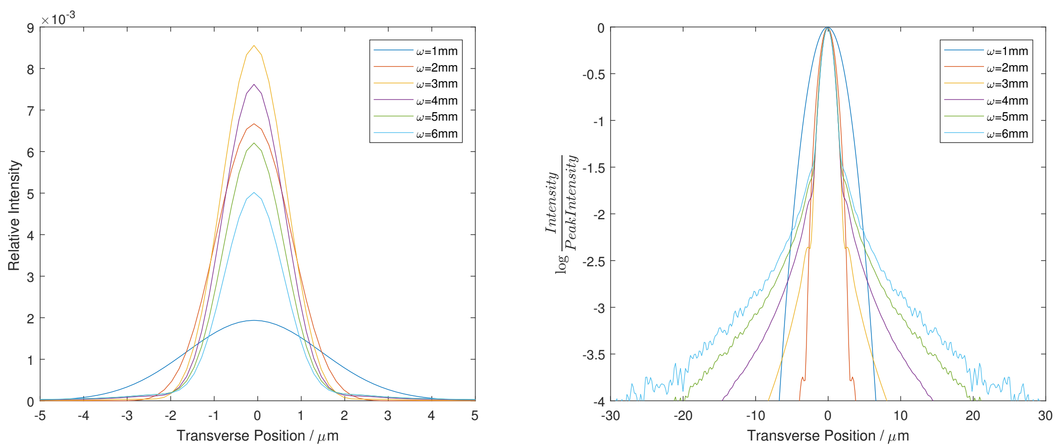

(a) (b)

Figure 5.2: Plotted are the intensity cross sections through the waists of simulated Gaussian beams, each containing equal total power, with initial radius ω after passing through lens with focal length $f = 25\,\text{mm}$ and finite radius $a = 12.5\,\text{mm}$. Increasing ω initially decreases the spot size while increasing the peak intensity, but where ω stops being small compared to a, the spot size stops improving, and the peak intensity decreases, as diffraction effects become more important. This causes the spot to stop being Gaussian, as more power is contained within sidelobes. Figure 5.2a shows each intensity relative to the highest intensity across all beams, while figure 5.2b shows the logarithm of the intensity of each beam relative to the individual peak intensity of each beam, making the sidelobes more clear.

5.1.2 Effects of Off-Axis Lenses

A second type of aberration is known as comatic aberration. This is aberration due to the optic axis of a beam not being colinear with the axis of the lens itself and is named for the apparent similarity of the resulting distortion in the image with the tails of a comet. Figure 5.3 shows the gradual deformation of the spot as the input beam to the same $f = 25$ mm, $a = 12.5$ mm is moved further from the axis.

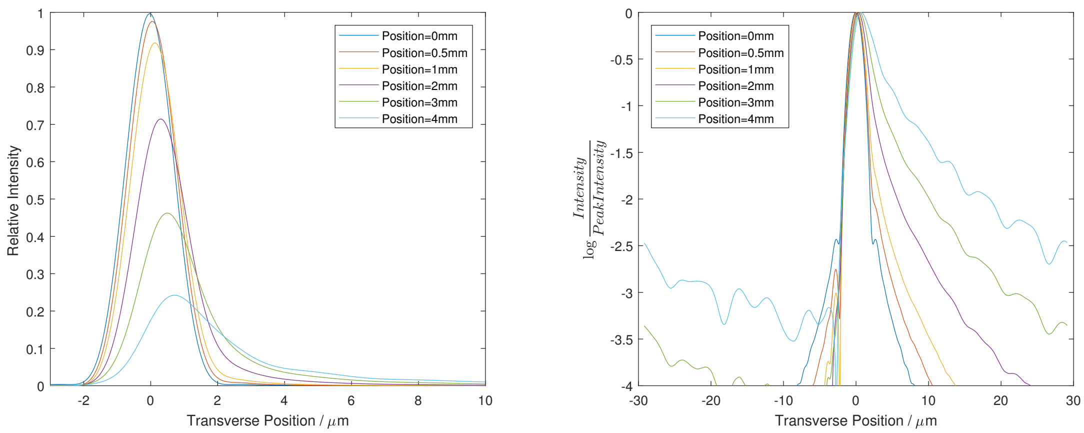

(a) (b)

Figure 5.3: Plotted are the intensity cross sections through simulated Gaussian beams, each containing equal total power and having the same size before a lens with $f = 25$ mm, $a = 12.5$ mm. The centre of each simulated beam enters the lens at some position, displaced from the centre of the lens by different amounts. As the initial beam moves further off axis, the resulting beam becomes more skewed, with reduced peak intensity, and a large tail.

This effect can be reduced by using an aspheric lens, but in general it is clear that to optimally focus a Gaussian beam, the centre of the beam should enter the lens within at most 0.5 mm, and similarly, at an angle of at most 0.5° to the optic axis of the lens.

5.2 Designing an System of Lenses

The aim of this section is to design a system of lenses that will achieve single ion addressing by focusing the row of beams emitted by the MC-PCF into a row of spots. Since each beam in the MC-PCF can be controlled individually by the AOMs, individual ion addressing is achieved by then trapping a string of ions such that one ion is within each spot. The design of the system is shown schematically in figure 5.4. It consists of four lenses guiding the addressing beams which at 400 nm are shown in blue, and one or more additional lenses used to collect photons emitted by the ions for imaging, which, at 397 nm are shown in violet. In this section I describe how I chose each lens, and how I optimised their positions, using the optical propagation program ZEMAX.

We are motivated to use the same objective lens, as opposed to, say having a second objective lens on the other side of the ion trap for imaging, for several reasons. First, space inside the vacuum chamber is at a premium, and we may want to use this space to mount other optics, for example, if we wanted to instead drive the Calcium 729 nm transition. Secondly, the light from the addressing beam is in general much brighter than any light emitted by the ions, and this setup ensures that no light from the addressing beam can fall onto the sensor. Finally, the objective lens will eventually need to be mounted very precisely with a micro-positioner relative to the ion trap, and using only one lens inside the vacuum chamber eliminates the effort and considerable cost of doing this twice. Further, we want to use a singlet, as opposed to compound, objective lens, because the lens will be cooled inside the cryostat to 4 K. We might expect the lens to deform somewhat in the process, and a compound lens, with many internal surfaces, could crack or be damaged.

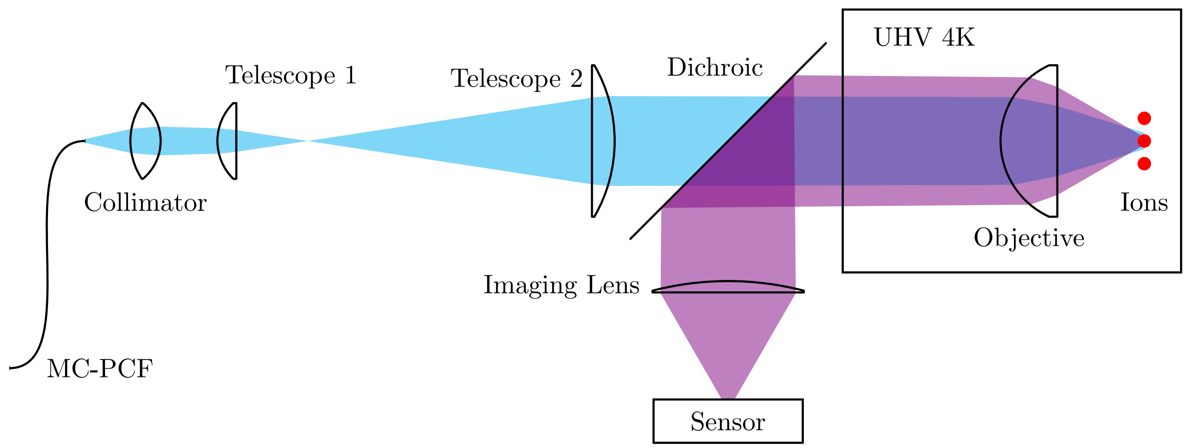

Figure 5.4: A schematic of the system of lenses I chose, with a rough guide to the dynamics of the addressing beams shown in blue. The aspheric Collimator lens collimates the diverging beams from the MC-PCF. The size of the beam is then magnified by a Telescope and then tightly focused by the Objective lens. Shown in violet is light emitted by the ions, collected by the Objective lens and the separated from the addressing beams by a dichroic mirror, before being focused onto a sensor for detection.

We can identify several criteria which the design must achieve, that will lead to a choice of lenses. First, we want to quickly be able to perform quantum gates on our ions. As we saw in equation 1.4, the Rabi frequency of a stimulated Raman transition is proportional to the square of the electric field amplitude at an ion, or equivalently, proportional to the optical intensity. As we saw in equation 2.14, a more tightly focused beam, that is, a beam with a smaller waist radius ω_0, has a higher intensity at its centre. Therefore the task of maximising the intensity is the same as focusing the beams as tightly as possible.

Secondly, if ions are to be addressed individually and independently, it should be the case that each beam should produce as small an intensity as possible at all ions except for the chosenone. Otherwise to drive a transition in one ion would be to drive transitions in adjacent ions. I therefore aim for the spot spacing between beams is at least several times the radius of each spot, so that the residual intensity due to one spot, at the centre of a neighbouring spot, is small.

Thirdly, if the final lens of the system is to be used both for addressing and for imaging, then it must be chosen to be suitable for this purpose. Under imaging, the ion will emit photons equally in all directions. The numerical aperture of a lens is defined as

$$\mathrm{NA} = n \sin \theta_{\max} \tag{5.3}$$

where θ_{max} is the half-angle of the largest cone of light from the focus to be accepted by the lens and n is the refractive index of the surrounding medium, with $n = 1$ in the case of a vacuum. To maximise the imaging efficiency therefore, the objective lens must have as large a numerical aperture as possible, in order to collect as large a fraction of the fluorescent photons as possible.

5.2.1 Being wary of the Ion Trap

The trap that will be used in the intended experiments is the High Optical Access Trap 2.0 (HOA2) from Sandia National Laboratories. It is a micro-fabricated surface trap, with a slot through the centre below the line of the centre of the trapping potential where the ions would be held. It is intended for the ion addressing beams to propagate normal to the surface of the trap, focusing on the ions and then passing through the slot. For this purpose, the slot has a numerical aperture of NA $= \sin\theta = 0.25$ where θ is the angle at the ions between the normal to the trap and the edge of the slot. Some of the power of the addressing beams will therefore go into the trap. This is undesirable, for example because it would cause heating in the trap, cause light to be scattered, or cause charging in the trap electrodes. Assuming the addressing beams expand from a minimal radius ω_0 at the ions, the fractional power hitting the trap is plotted in figure 5.5. It shows this for both an ideal Gaussian beam, and a example of an imperfect Gaussian beam, with $M^2 = 1.8$ following the measurement in section 4.3. This thus provides a lower bound on the possible beam waist at the ions of approximately 1 µm.

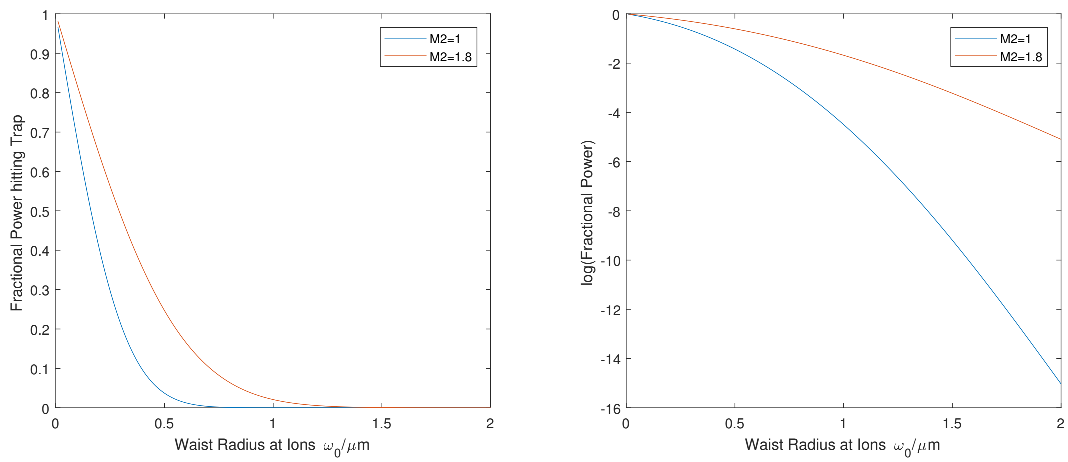

(a) (b)

Figure 5.5: Plotted is the fraction of the power of a beam that hits the HOA2 trap as it passes through the slot below the ions, both for an ideal Gaussian beam, and for a beam containing higher order modes according with equation 2.6, with $M^2 = 1.8$ as measured in section 4.3. This assumes an addressing beam with its narrowest point ω_0 centred on the ions. The power hitting the trap becomes small for $\omega_0 > 1$ µm.

5.2.2 Choosing an Objective Lens

A suitable choice of objective lens is crucial, as it pertains most directly to the first and third of the design criteria. Due to its location inside the vacuum chamber it also has the most constraints that limit the possible choices. As stated, it should have as large a numerical aperture as possible to maximise photon collection for ion imaging. Similarly, given the inverse relationship between the size of a Gaussian beam when focused and when collimated seen in equation 5.2, it should be large in diameter to receive a large collimated addressing beam and strongly focusing to focus it to as small a spot size as possible. Likewise, to minimise the spot size, the lens should have as short a focal length as possible. Since we intend to use the entire diameter of the lens for both addressing and for imaging, an aspheric lens will be required.

The choice is limited however by several factors. First, the magnetic field at the ions is generated by superconducting coils around them. These limit the available physical space for a lens, and would also obscure the addressing beams and imaging light. As such the diameter of the lens chosen could be at most 30 mm, including a mount. Secondly, in addition to the addressing beam, several other beams would be incident upon the ions, for example beams at 397 nm for EIT Cooling [49] for ion fluorescence. The cooling beams are to be at 45° to the axis of the addressing beams. These beams cannot be incident upon the objective lens, because it would either prevent their function, or possibly allow their light to be mistaken by the imaging sensor for light from the ions. This means that back focal point of the lens, being the distance between the flat surface of the lens, and the focal point where the ions are, must be greater than the radius of the lens.

A lens was found that met these requirements. It was from Edmund Optics, Stock #84-338. It has a diameter of $d = 25$ mm, a focal length of $f = 25$ mm and a numerical aperture NA $= 0.5$.

5.2.3 A Possible Imaging System

In this section I give a design for a system that could be used to image the ions. The fine details of what would be required of such a system were not known at the time, for example I don't know exactly what sensor will be used to detect light from the ions. Therefore I present only a plausible system, detailing the features that affect the design of the addressing system, and keeping general the features which are not essential and are subject to change.

The light from the ions at 397 nm is separated from the path of the of the addressing beam using a dichroic mirror. A dichroic mirror, Semrock #TLP01-448, the transmission of which is sharply dependent on the angle of the incident light. Figure 5.6 shows the transmission and reflectance of the mirror at different wavelengths. At 58° we can maximise the reflectance of the 397 nm imaging light while minimising disturbance of the 400 nm addressing beams.

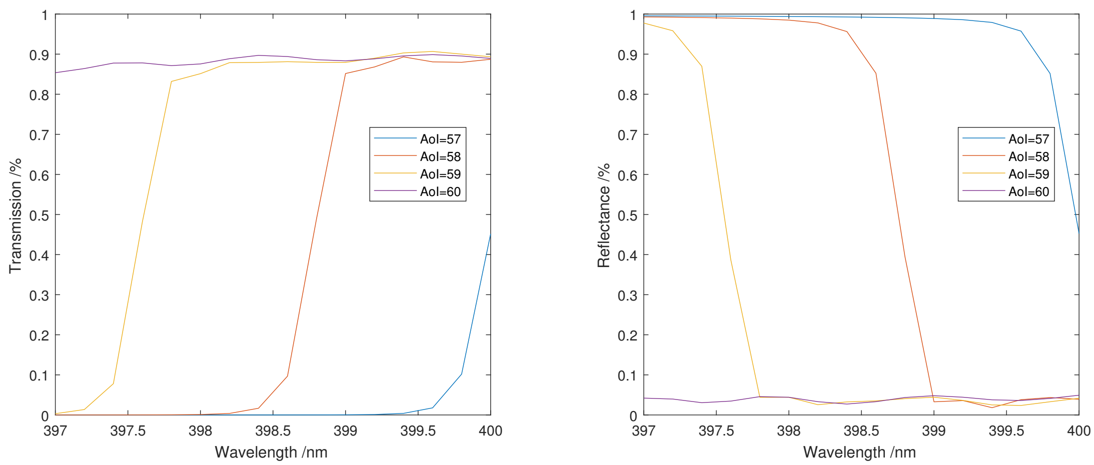

Figure 5.6: Plotted are the reflectance and transmission of the Semrock dichroic mirror. Visible is the sharp change in transmission over a narrow range of wavelengths between the imaging wavelength of 397 nm and the addressing wavelength of 400 nm. The cutoff wavelength depends strongly on the angle of incidence (AoI) of light on the dichroic. Data taken from Semrock.

What is known however, is that the imaging system must be able to resolve ions in the object plane spaced by several microns. This means that the spot size in the image plane will be much smaller than the spacing between the spots, and this spacing should be at least several times the resolution of the sensor. A pixel size for the sensor was given as 12 µm. Further, it is required that ions be at or very close to the focus of the objective lens. Treating the ions as point sources, this means the imaging light will become plane waves after the objective lens. This has several advantages. First, since we need the imaging system to collect light as efficiently as possible, and given the strong dependence of the reflectance of the dichroic on the angle of incident light, plane waves maximise the reflectance efficiency of the dichroic. Secondly, plane waves minimise the dependence of imaging system on the distance between the dichroic and the objective lens. This distance may vary, depending on how the imaging system is mounted, and also because the vacuum chamber and cryostat, containing the ions and objective lens but not the dichroic, is suspended like a pendulum, and so its position may oscillate. Thirdly, it means that the remainder of the imaging system can just be a simple telescope with the object at infinite distance.

Figure 5.7 shows a ZEMAX model of such an imaging system. It shows at cone of light from the ions, accepted by the objective lens, reflected by the dichroic, magnified by a telescope and finally focused onto a sensor by a second objective lens. For the purposes of demonstration simple lenses are assumed for all except the initial objective lens. The system is summarised in table 5.1

Such a system gives a magnification of approximately $M = 25$, with an Airy radius at the image plane of 16 µm. Defining a field of view to be the region of the object plane where size of the central peak of the Airy function at the image plane is less than double the minimal value, I estimate a field of view with a diameter

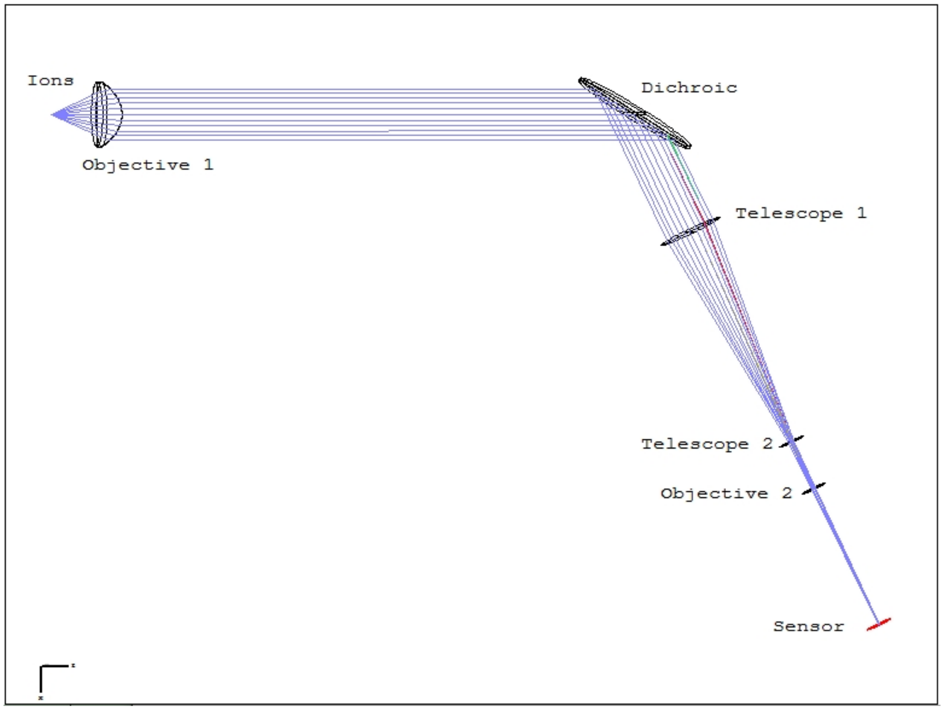

Figure 5.7: The layout of a possible imaging system, showing light from the ions collimated by the Objective lens chosen in section 5.2.2, reflected by a dichroic mirror, magnified by telescope 1&2 and focused onto a sensor by a second objective lens.

of 80 µm. Figure 5.8 shows a spot diagram at the sensor, giving a qualitative idea of what an image might look like. It shows an image of 7 ions, each spaced by 6 µm. Such a setup would give well resolved spots spread over around 1000 µm.

5.2.4 Optimising the Addressing System

Having chosen an objective lens, several lenses must still be chosen and their relative spacing optimised. This optimisation, and subsequent simulation was performed with the program ZEMAX. First, as stated, the goal is to maximise the intensity of the addressing beam at an ion while minimising crosstalk from the intensity at an ion due to the beams addressed to the adjacent ions. That is to say, the radius of each beam spot at the ions must be small compared to the spacing between the spots. Given an allowed threshold for a ratio between the crosstalk intensity and the addressing intensity of 10^{-4} and assuming an approximately

Component	Focal Length f/mm	Spacing l/mm
Ions		17.862
Objective 1	25	200
Dichroic		25
Telescope 1	100	90
Telescope 2	-10	20
Objective 2	75	58.074
Sensor		

Table 5.1: Tabulated are the components of the imaging system. Focal lengths are shown where applicable, and the spacing given is the distance to the next component. The spacing between the ions and the objective lens is of particular importance, as it constrains the design of the addressing system, since the two systems share this lens.

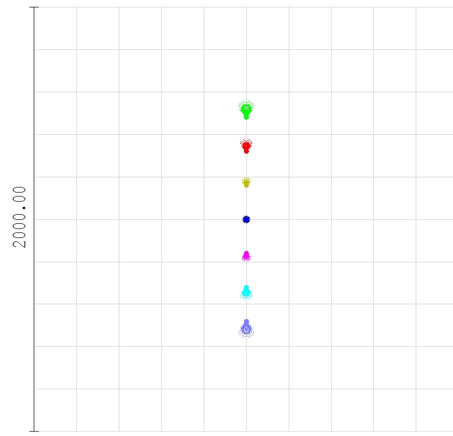

Figure 5.8: A spot diagram simulating the images of astringof seven ions. For evenly spaced ions spaced 6 µm apart, shown are the well resolved spots. The total height of the image shown is 2000 µm

Gaussian spot according to equations 2.13 and 2.14 with an field distribution $E(r)$ or intensity distribution $I(r)$ of

$$|E(r)| \propto e^{-\frac{r^2}{\omega^2}} \qquad I(r) \propto e^{-\frac{2r^2}{\omega^2}} \tag{5.4}$$

the ratio between the spacing between spots d and the spot radius ω is limited to $\frac{d}{\omega} > \sqrt{2\ln 10} = 2.2$. We see here an advantage of the $^{40}Ca^{+}$ Raman qubit over the Optical qubit described section 1.2. From equations 1.4 and 1.3, the Rabi frequency of the Raman qubit depends on the intensity and the the Optical qubit on the electric field amplitude. As such the limit for the Optical qubit is $\frac{d}{\omega} > \sqrt{4\ln 10} = 3.0$. We must remember however that the spot may have some side lobes due to aberrations and due to the initial beam from the MC-PCF containing modes other than the fundamental mode, this limit is soft and should be viewed generously. Under simulation, it can be seen if a potential design has the required crosstalk.

Secondly, for a lens to produce a sharply diverging, and hence tightly focused, Gaussian beam, requires it to receive a wide, well collimated beam with a low divergence. This further constrains the addressing system. Having a beam with a low divergence prior to the objective lens has another benefit. As with the imaging system, it is desirable to have the addressing system insensitive to the spacing between the objective lens and the second telescope lens. This is because this distance may be subject to change, first of all because space is needed to mount all of the equipment close to the vacuum chamber, and secondly because the position of the vacuum chamber may oscillate.

However, the beam cannot be arbitrarily large and have an arbitrarily low divergence, as the physical choice of objective lens has a finite radius of $a = 12.5$ mm. A beam with a radius ω that is not smaller than the radius of the lens suffer distortion as seen in section 5.1.1. Crosstalk becomes significant, and focusing stops improving, for ratios above approximately $\frac{a}{\omega} > 4$. Therefore the mode at the objective lens should be have a radius of around $\omega = 3.1$ mm. This means we are aiming for a focused spot at the ions with radius $\omega \approx 1$ µm. This is fortunate, as it also means that the fraction of the beam power that will hit the HOA2 trap after passing the ions is small, at most 2 % as seen in figure 5.5. Again, the exact tolerable limit of these values can be found under simulation.

Finally, it is important to note that manipulating multiple beams from the multiple cores of the MC-PCF presents certain challenges. For symmetry reasons, the addressing system is designed with the central core of the MC-PCF parallel to, and centred on, the axis of the lenses. Of course, necessarily the other 6 cores are displaced from this axis, and the addressing beams from them will be likewise displaced. As the beams progress through the system, they will in general not pass through the centre of each lens, nor normal to their surfaces. As seen in section 5.1.2 they will therefore suffer aberrations at at each surface, which reduce their peak intensity at the ions and would lead to increased crosstalk. The addressing system was therefore designed to try to keep the beams close to the optical axis of the system, and to have their propagation axis at small angles to it.

A major possible example of this issue is shown schematically in figure 5.9. The first telescope lens could be concave lens as opposed to a convex lens, with an equal, but opposite, focal length. With a suitable change in spacing between the telescope lenses, the effect on the central beam could be made to be the same giving a mild advantage by having a shorter overall length required for the addressing system. However, for the off-axis beams, a defocusing lens could have the effect of magnifying the angle between the beam and the optic axis, causing the beam to hit the next lens far from its axis. This would cause significant spherical aberration, and could cause a substantial fraction of the power of the beam to be clipped by the edge of the lens. Conversely, a focusing lens has the opposite effect, keeping the various addressing beams approximately parallel and with a large degree of overlap. Designing a suitable addressing system is clearly easier therefore if all beams are kept close together, so that the action of the lenses on each of them is approximately the same.

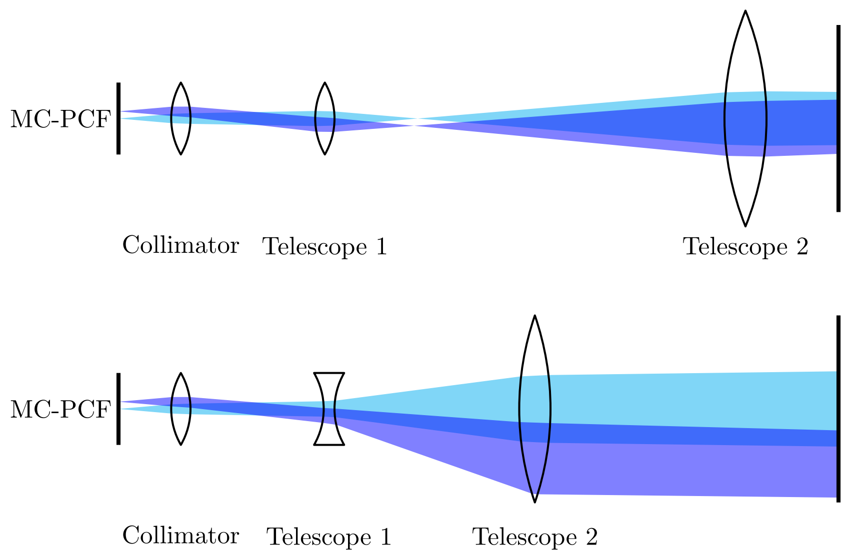

Figure 5.9: Shown are schematic images of two possible addressing setups. Show in light blue is an on-axis beam, in dark blue an off-axis beam, starting from the MC-PCF and passing through the first three lenses of the addressing system shown in figure 5.4. The top image shows a Keplerian style telescope with two focusing lenses, keeping the beams overlapping and close to the main axis. The bottom image shows a Galilean style telescope, with a defocusing then a focusing lens, which, while shorter, leaves the off-axis beam susceptible to aberration and beam clipping.

Given these constraints, a design was chosen. A collimator lens Thorlabs F671APC-405 was chosen to reduce the divergence of the beams from the MC-PCF. Then the telescope lenses were chosen to match the beam after the collimator to the large beam to be received by the objective lens. The system is summarised in table 5.2. Figure 5.10 shows a diagram of the same addressing system, with the dimension perpendicular to the beams exaggerated by a factor of 20. For a sense of scale, lines representing the 7 addressing beams are shown, with each colour representing a different beam for clarity. These lines approximately trace the surface within the beams on with the electric field amplitude falls to e^{-1} times the maximal amplitude for a give position along the beam axis, assuming perfect beams from the MC-PCF containing only the fundamental mode and so with $M^2 = 1$. Visible is that the beams achieve several of the design criteria previously given, such as that all beams remain close to the central axis of the lenses, and that the beams beam radii are several times smaller than the radius of the lenses at every surface.

5.3 Simulating the Addressing Beams

I simulated the effect of the system of lenses chosen in the previous section on beams emitted by the MC-PCF. To do this I used the ZEMAX Physical Optics Propagation software, which coherently calculates the

Ideal Component	Real Component	EFL f/mm	Spacing l/mm
MC-PCF	MC-PCF		5.166
Collimator	Thorlabs F671APC-405	4.02	29.729
Telescope 1	Thorlabs AL1225-A	25	460.040
Telescope 2	CVI Optics PLCX-25.4-360.6-C-400	700	250.000
Objective	Edmund Optics 84338	25	17.862
Ions	Ions		

Table 5.2: A summary of the components of the addressing system. Spacing is the distance to the next component, focal length is given where applicable. The ideal component names correspond to figures 5.4 and 5.10 while the real component are the model numbers of the purchased lenses.

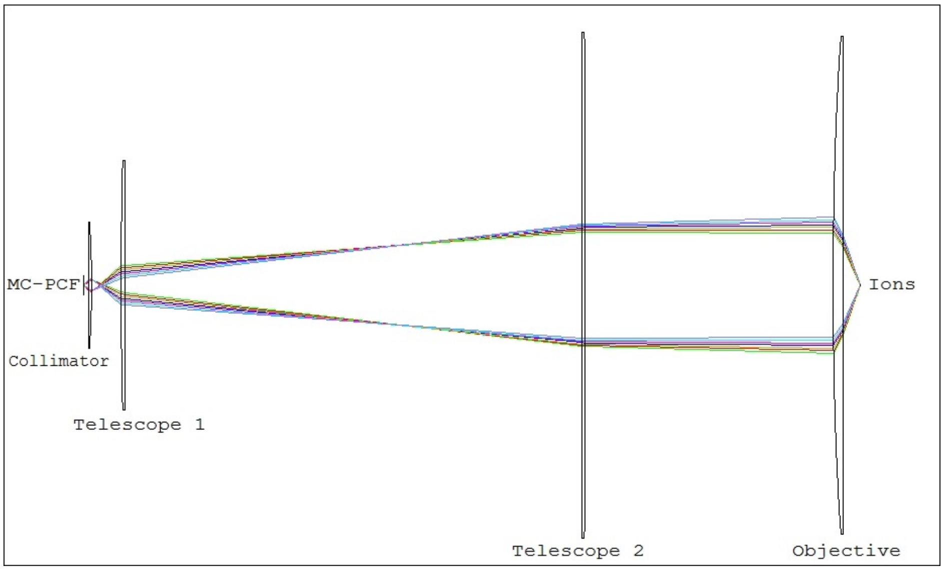

Figure 5.10: The design of the addressing lenses system, as detailed in table 5.2. Just about visible are 7 beams represented by seven colours, the lines following the surface of the beam where the electric field amplitude falls to e^{-1} of the its value on the beam axis. All beams are well contained within the radius of the lenses, and close to the axis of the system, to reduce aberrations in the final spot at the ions.

propagation of electric fields through spaces. This ability is important as we expect phenomena to occur that are not captured by the geometric optics used by the base ZEMAX package, nor its Paraxial Gaussian Beam package.

We expect there to be aberrations caused by the edges of the lenses, which are not considered by the Paraxial Gaussian Beam model, which assumes an ideal beam at every surface. Likewise, we expect some comatic aberration caused by beams other than the central beam propagating at some angle to the optic axis of the lenses.

Further, we worry that that the beam is not entirely in the fundamental mode. Indeed, we know this to not be true, as in chapter 4 we measured the divergence of the beams from the MC-PCF to differ from ideal Gaussian beams by a factor of $M^2 = 1.8$. The Physical Optics Propagation package gives us the ability to simulate the propagation of higher order modes, or any arbitrary combination thereof.

Thus I calculated the the beam intensities in the plane containing the ions. I did this for initial fields that were ideally Gaussian, based on the mode radius $\omega = 2.8\,\mu\text{m}$, and for initial fields that contained the ideal mode, and randomly generated combinations of higher order modes, that gave overall beams with the measured value of M^2. I plotted the cross section through the calculated intensity along the line containing the peak intensities, where the ions would be located. In figure 5.11 plotted is the intensity distribution for the ideal Gaussian beam and in figure 5.12 is the result for the imperfect beams. For the sake of simplicity, and since the lens system is rotationally symmetric, I simulated only the central beam and the 3 cores on

Beam	Ideal $M^2 = 1$ $\omega_0/\mu m$	$M^2 = 1.8$ $\omega_0/\mu m$	Position $y/\mu m$
4	1.13	1.00	0
5	1.13	1.07	5.8
6	1.18	1.22	11.6
7	1.29	1.25	17.5

Table 5.3: Tabulated are the spot sizes at the ions, estimated by measuring the radius at which the intensity falls to e^{-2} of the peak intensity, for an ideal and $M^2 = 1.8$ Gaussian beam. The imperfect beam spot sizes vary with the randomly generated imperfect beam, but are representative. As seen in figure 5.2a they are slightly smaller than the ideal beam spots, as they have been focused from a larger beam prior to the objective lens. They have a correspondingly larger crosstalk seen in table 5.4.

$M^2 = 1$ Ideal Beam	Relative Intensity at Ion			
	4	5	6	7
4	-	1.4×10^{-5}	1.9×10^{-7}	9.8×10^{-9}
5	9.9×10^{-7}	-	5.3×10^{-5}	1.8×10^{-6}
6	1.7×10^{-8}	2.5×10^{-8}	-	1.1×10^{-4}
7	8.8×10^{-8}	5.8×10^{-7}	7.7×10^{-7}	-
$M^2 = 1.8$ Imperfect Beam	Relative Intensity at Ion			
	Central	1	2	3
4	-	1.4×10^{-3}	1.2×10^{-4}	9.1×10^{-6}
5	4.1×10^{-6}	-	2.2×10^{-4}	6.2×10^{-5}
6	8.8×10^{-9}	3.4×10^{-8}	-	7.5×10^{-4}
7	1.67×10^{-6}	3.3×10^{-5}	5.4×10^{-4}	-

Table 5.4: Tabulated are the intensities of each beam, at the position of the peak intensity of other the other beams, giving an estimate of the crosstalk between ions. All crosstalks for ideal beams are less than the threshold of 10^{-4} for ideal $M^2 = 1$ addressing beams, and are slightly above this threshold for a real $M^2 = 1.8$ beam. Values for the imperfect beam are approximate but typical; each beam was simulated using a randomly generated initial beam and show would vary between simulations. Since the system is symmetrical, only half the beams are tabulated, with the beam labels counting outward from the centre.

the right side of the MC-PCF, with the plotted left side results merely reflections of these, included for completeness.

Thus the lens system, at least theoretically, does what was required of it. A row of seven addressing beams from the endface of the MC-PCF is focused to a row of well defined spots at the ions. Figures 5.11 and 5.12 show only relative intensities, with the physical peak intensity depending on the total power contained in the beam, which of course can vary. The fraction of the total power that reaches the ions is at least 99 %, so the physical intensity can be estimated from the relative intensity, the total power and the spot radius. The peak relative intensity for the ideal beams decreases as the beams move further from the central beam. This is because they are more subject to aberrations at the lenses, and so their main peaks become wider, and some of their power is contained within sidelobes. For the imperfect beams, the peak intensities show somewhat more variation. This is partly because these beams are wider at the collimated stages of the addressing system, and so some of their power is clipped by the edges of the lenses, but mostly because their imperfect nature means that their true peak intensity is either slight before or behind the ion plane, or is shifted slightly off of the ion axis through along which figure 5.12 is plotted.

Table 5.3 summarises simulated spot radii ω_0 and spot positions for the ideal beams, estimated by measuring the width at which the intensity falls to e^{-2}. We note that since the system was designed to cope with a certain amount of deviation from ideal Gaussian beams. However, we can see that the higher order modes causes some deviation from Gaussian spots, most visible near the base of the curves. This leads to more significant crosstalk, as summarised in table 5.4. Since the system is symmetrical, I show only data for the 4 right-most beams, as depicted in figures 5.11 and 5.12.

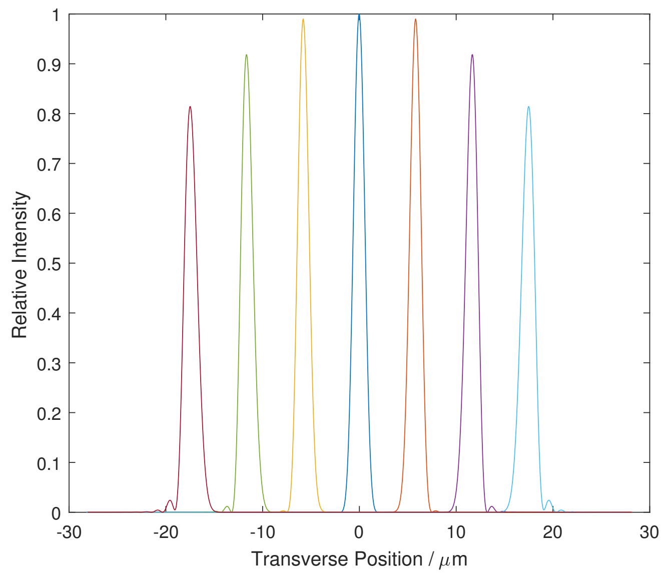

Figure 5.11: Plotted are cross sections through the addressing beams in the ion plane, assuming ideal beams at the MC-PCF. Different beams from different cores are represented by different colours. The spots grow in width as they move from the the central beam, and so show a reduced peak intensity. Furthermore, some power is contained within sidelobes adjacent to the major peaks pointing away from the centre, due to comatic aberration. Nevertheless they are well resolved from each other, with little overlap, leading to little crosstalk. Since the lens system is symmetrical, the plot has mirror symmetry about the origin.

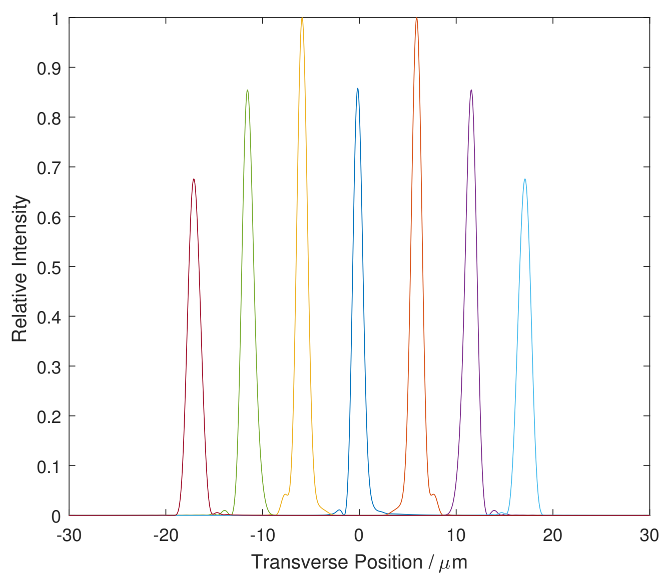

Figure 5.12: Plotted are again cross sections through simulated addressing beams, this time with imperfect initial beams. Notice that the peaks do not show a large increase in width, as the system was designed to tolerate a certain level of imperfect, so the beams are still tightly focused. However, there is somewhat more variation in the peak intensities due to the true peaks being off the axis. Higher order modes give distortion near the base of the peaks, leading to higher crosstalk.

5.4 Building the System

Having designed and simulated the addressing system, I purchased components and constructed it. Each lens was mounted and the mounts bound together by a cage. This helps to ensure that the same axis passes through the centre of each lens. In a final experimental setup, of course the objective lens is mounted inside the vacuum chamber and so would not be physically linked to the other lenses. In this scenario however, it would be mounted on a translation stage, which could instead by used to provide alignment. For my construct however, I included all four lenses in the same cage for convenience.

Since the lenses were assembled by me by hand, certain limitations on their accurate positioning are obviously present, well beyond the precision of the positions given in table 5.2. A reasonable estimate would be that uncertainty in the position of the lenses is at least 1 mm. As it was designed for, the beam spots at the ions were insensitive to the distance between the objective lens and the second telescope lens varying by tens of centimetres. Likewise, the distance between the two telescope lenses, could vary by a few centimetres. The distances between the collimator and the first telescope lens, and between the MC-PCF and the collimator, were found however to have much lower tolerances, with errors in position of approximately 100 µm leading to a halving of the peak intensity at the ions. Under simulation however, that errors of up to 1 mm in the collimator-telescope distance could be corrected for by fine control of the the distance between the collimator and the endface of the MC-PCF. For this reason I bought a micrometre mount for the collimator lens, which could move the lens along the optic axis with micrometer accuracy.

For mounting the MC-PCF I acquire a V-groove with a magnetic clamp. I knew that the position of the initial beam relative to the axis of the system affects the propagation of the beam, hence the variation between spots seen in figure 5.11. The position of the centre of the MC-PCF relative to the axis of the collimator lenses must be known at least to with around 10 µm. For this reason I bought an x-y translation mount into which the V-groove could be mounted. It had the ability to move MC-PCF horizontally and vertically to ensure that it was properly centred. Furthermore, the V-groove mount meant that rather than twisting the MC-PCF, which is small, delicate and difficult to handle, the whole mount could be rotated and locked in position. This means that the row of cores of the MC-PCF that contained light can be orientated as desired. For convenience, I chose to have this row be horizontal, such the the MC-PCF would be orientated as shown in figure 4.2.

To further ensure that the lenses were properly aligned I used an adjustable iris that could be mounted with lenses to see if the beams were passing through the centre of the lenses. Similarly, to ensure the beam were well aligned, I shone the beams onto a piece of card distant from the lenses, to ensure that the beam followed straight line parallel to the axis of the system.

5.5 Characterising the System

In this section I explain how I attempted to characterise the system I built. Specifically, I wanted to measure the size of the beams in the place where the ions would be, for real beams from the MC-PCF. Since they were expected to be approximately 1 µm in radius, they were too small to measure using the Beam Profiler that I used in earlier chapters.

5.5.1 Using a Knife Edge

To measure the spot size therefore, I mounted a knife edge vertically onto a translation stage. The translation stage could be moved with micrometre precision in three directions. I positioned the knife edge close to where the waist of the addressing beams was, where the ions would be. Behind it I placed a photodiode in the path of the addressing beams. When the knife edge was far from the beams, the photodiode would record the total power contained in the beam. By translating the knife edge through the beam, some of the power would progressively be prevented from reaching the photodiode, until the entire beam hit the knife edge, and the photodiode records nothing. Assuming a perfectly Gaussian beam shape, the power P reaching the photodiode is given by

$$P(x) = P_{\text{total}}\sqrt{\frac{2}{\pi}}\int_{-\infty}^{x} e^{-\frac{2u^2}{\omega^2}}\,du = \frac{P_{\text{total}}}{2}\left(1+\text{erf}\left(\frac{\sqrt{2}x}{\omega}\right)\right) \tag{5.5}$$

where P_{total} is the total power contained in the beam, x is the position of the knife edge, with the solid part of the knife extending in the positive x direction, ω is the beam radius at the position of the knife edge and $\mathrm{erf}(x)$ is the error function. Thus, by using a knife edge and taking measurements as described, the radius of a Gaussian beam can be estimated by fitting the results to an error function.

Figures 5.13a and 5.13b respectively show the simulated results of such a measurement using ideal Gaussian beams and an imperfect beam as described in section 5.3. In the ideal case, the simulated results of course are very close approximations of error function curves. However, in the imperfect case, while we still see a steep region at the centre of the spot, the longer tails at the top and bottom are the result of the higher order modes and aberrations in the addressing beams.

However, the measured results were qualitatively as predicted, but showed significantly larger spot sizes than predicted. The data from the knife edge measurements are plotted in figure 5.14.

There are several possible sources of these significant differences, both between the measured and simulated data, and between the measured data for each core. Certainly the beam is far further from the ideal case that I had made allowance for based on my measurements of the beams from the MC-PCF in section 4.3. To take these knife edge measurements, I coupled light into each core directly, also as described in section 4.3. This is a significant source of possible error.

First, with the MC-PCF locked into the lens cage, it is no longer possible to use a Beam Profiler to view the beams that come from it, and so it is difficult to optimise the coupling of light primarily into the fundamental mode of each core. Alternatively, cutting the MC-PCF was unreliable and the endface was very sensitive to damage, which could significantly distort the beam, even with perfect in-coupling.

Possibly light was being coupled also into multiple cores, as is suggested by plotting the spatial derivative of the knife edge measurement data. Assuming that the beam shape along the vertical axis, perpendicular to the horizontal axis used for the knife edge measurements, is constant, we can take this to be proportional to the intensity as simulated in figures 5.11 and 5.12. This derivative is plotted in figure 5.15.

Finally, the aberration could be caused by misalignment in the lenses. This is also made plausible by the data, as one tail of the error function is longer than the other for several cores, but always on the same side. This is not true for all cores however.

It is also possible that I was not translating the knife edge through the narrowest point of the beams. For a predicted beam radius of around $\omega = 1.1\,\mu\mathrm{m}$, from equation 2.10 we predict a characteristic length of the beam waist to be $z_R = 9.5\,\mu\mathrm{m}$. Thus I repeated the knife edge measurement through a beam through a range of positions z along the length of the beam close to the focus. Figure 5.16 shows the results of these measurements. The lowest value of the beam radius ω that was found was $8.2\,\mu\mathrm{m}$. Thus not significant improvement was found and I was confident that the earlier measurements were at, or very close to, the true narrowest points of the beams.

5.5.2 Using a Rotating Disk

With the method described in the previous subsection, it is still impossible to control for some of the possible problems in the measurement of the beam size at the ions.

We still don't know if the light being coupled efficiently into just one mode of just one core of the MC-PCF. The section of free MC-PCF that I had left was very short, and so aligning the end that was receiving light from the laser caused misalignment in the end fixed into the addressing system, and vice versa. Further, the process of moving the knife edge and taking readings was very slow. This means the it was very difficult to reposition components and see what effect it had.

It is also possible, indeed likely, that the system is subject to some vibrations. If the beam is oscillating relative to the knife edge, the measurement of the power that passes the edge is effectively an average over this oscillation, as the measurement take place on a timescale much longer than many sources of vibration. This would give a much larger effective spot size. I therefore sought a faster method.

I used an Optical Chopper (Thorlabs MC2000B and MC1F10). It is a rotating disk, with 20 equal sectors, which alternate solid and empty. I placed this disk in the plane of the ions, with the addressing beams passing through it, hitting a photodiode on the other side. By displaying the measurement of the this photodiode on an oscilloscope, a square wave such as that shown in figure 5.17 is seen. The high voltage regions correspond to the beam passing through an empty sector of the disk, the low voltage regions to the

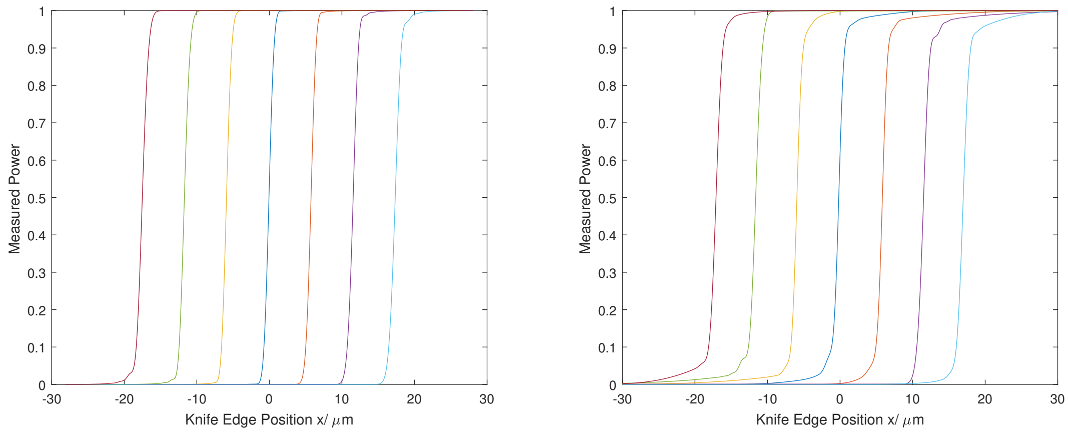

(a) (b)

Figure 5.13: Plotted are the simulated results of the described knife edge measurements. Figure 5.13a shows the results for ideal Gaussian beams, figure 5.13b shows them for imperfect beams with $M^2 = 1.8$. Both cases approximate error functions as described in equation 5.5 but the imperfect case shows somewhat longer tails. The measured power is given as a fraction of the total power in each beam.

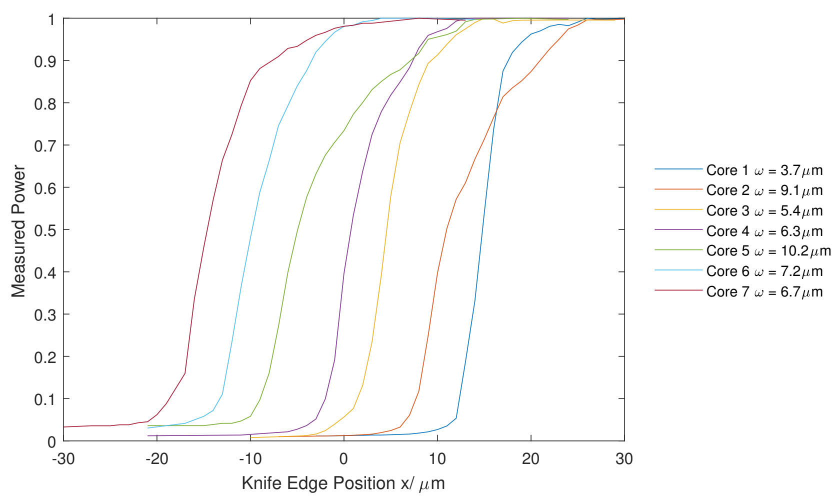

Figure 5.14: Plotted are the results of translating a knife edge through each beam and measuring the power that isn't obstructed by the knife at each position. Estimates of the beam size given were estimated by fitting each curve according to equation 5.5. Note the steep regions corresponding to positions of peak intensity in each beam, and the long tails, much longer than predicted, indicating a significant amount of deviation from an ideal Gaussian beam.

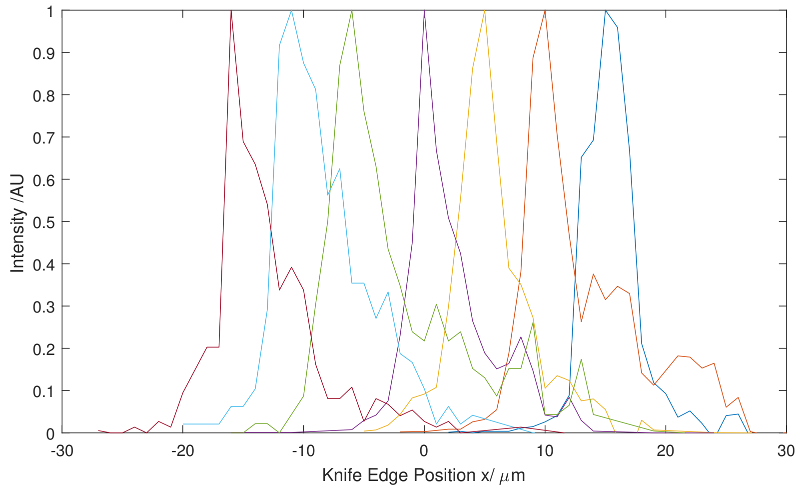

Figure 5.15: Plotted is the derivative of the data shown figure 5.14, which we expect to be approximately proportional to the beam intensity. Crosstalk is clearly significant and far higher than predicted. Several curves show secondary peaks underneath the main peak of the adjacent core. This could be due to multiple cores having light coupled into them.

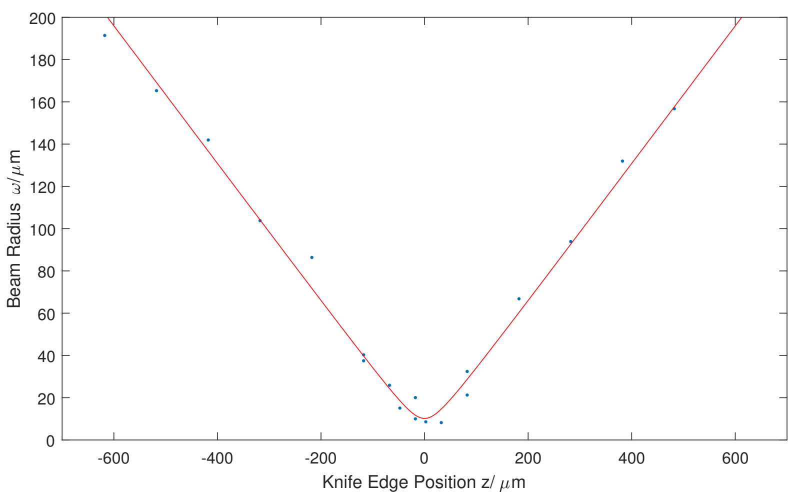

Figure 5.16: In an attempt to locate the true narrowest point of the beams, I measured the radius of one beam at several points along its length. No significant decrease in beam size was found compared to the earlier results and so I was confident that I had earlier been moving the knife edge through the true focal point.

beam hitting a solid sector of the disk. The transitions are where the edges between these sectors cross the beam, and so are equivalent to the knife edge measurements taken in the previous subsection.

This method allows the a measurement to be performed on a timescale of 10 µs, and so eliminates the effects of vibrations that have periods greater than this. It also allows for hundreds of measurements to be taken per second. By setting the oscilloscope to closely view the transition between the low and high voltage regions, the narrowest point of the beam can be found by moving the spinning disk to find the sharpest transition. Likewise, aligning the system is much easier, as the effects of any change can be seen immediately.

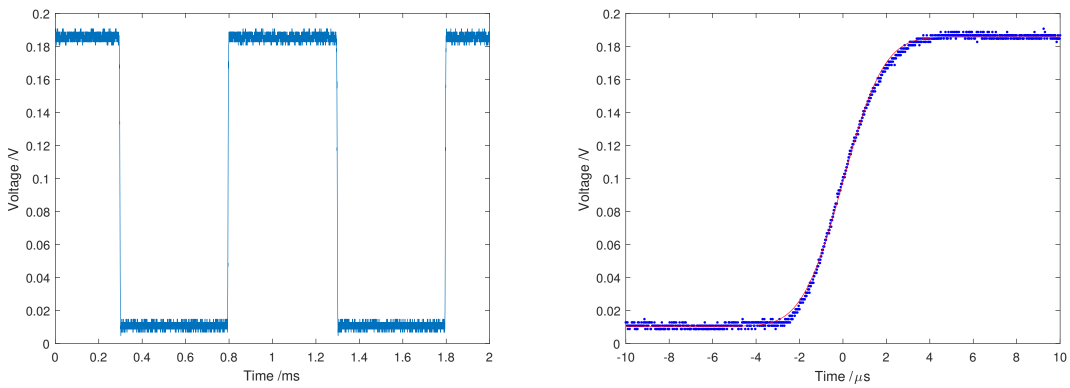

(a) (b)

Figure 5.17: Plotted are measurements of the voltage induced in a photodiode by an addressing beam, as it is repeatedly blocked by a spinning disk with alternating solid and empty sectors. The disk rotation frequency was 50 Hz, with 10 empty sectors per rotation. Figure 5.17a shows the ability to repeatedly take many measurements of the beam, while figure 5.17b shows a close up of the transition, fitted to an error function curve. This is later used to estimate a beam radius.

By this point, the Chiral Photonics product described in section 4.6 had arrived. This would hopefully eliminate the error involved in manually coupling light into the the MC-PCF. I connectorised one of the 405 nm input fibres, locked the free end of the MC-PCF into the addressing system and measured the spot size at the ions.

Using the method described, I recorded the transition between the two regions a hundred or so times consecutively. I fitted an error function to each of the these transitions (suitably adjusted for rising and falling transitions)

$$V = V_{\text{mid}} + \frac{\Delta V}{2}\text{erf}\left(\frac{\sqrt{2}t}{T}\right) \tag{5.6}$$

where V_{mid} is the midpoint of the transition, ΔV the height of the transition and T a characteristic duration of the transition. This characteristic duration can be related to the radius ω of the beam by the speed v at which the edge of the spinner passes through the beam

$$T = \frac{\omega}{v} = \frac{5\omega}{\pi R f} \tag{5.7}$$

where $R = 25$ mm is the distance of the centre of the beam from the centre of the rotating disk and f is the rotation frequency of the disk. In the hope being able to observe high frequency vibrations in the beam spots, I did this for a range of rotation frequencies. It was noticed that successive measured values of T, and hence of ω, oscillated with the same frequency as the rotating disk, for all chosen values of the rotation frequency f. This could be explained by a slight wobble in the position of the disk, such that it sometimes passes through the waist of the beams, and sometimes is displaced from the waist, where the beam radius is larger according to equation 2.7. Thus the lowest measured value from each cycle was taken to represent the true beam spot size ω_0.

Figure 5.18 shows a plot of the transition time T and the inverse of the frequency. By fitting this to a line through the origin, the beam radius $\omega_0 = 7.2\,\mu\text{m}$ can thus be estimated. Vibrations in the addressing system would cause an apparent broadening in the spot size, and hence an increase in the transition time, at lower rotation rotation frequencies. We do not see this, and so, I conclude that such vibrations are not a significant source of error. Indeed, we see the opposite; it can be seen that at high frequencies, the transition time stops decreasing, tending towards around $2\,\mu\text{s}$. This is likely due to the response time of the photodiode becoming comparable to the transition time. This limited my ability to test for high frequency vibrations with periods close to $2\,\mu\text{s}$.

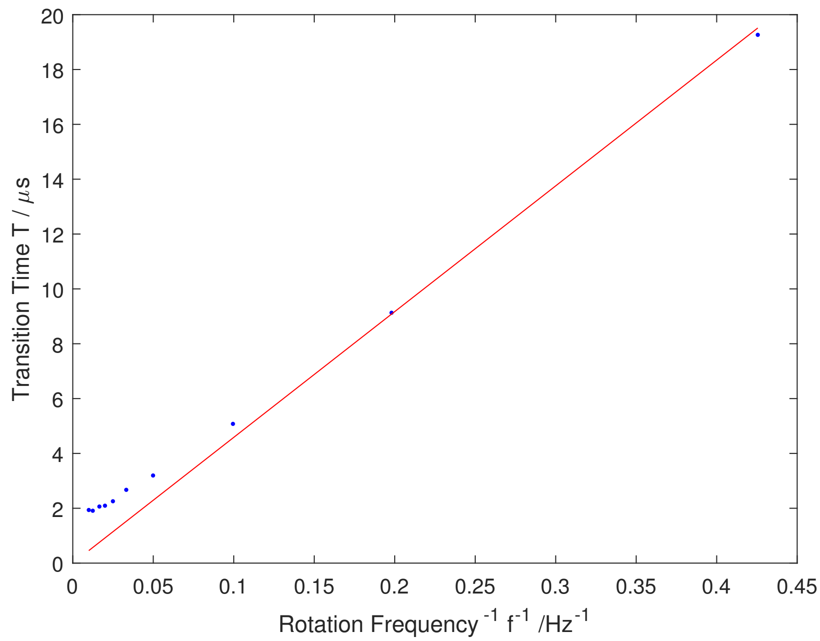

Figure 5.18: Plotted is the measured transition time T between a fully blocked addressing beam, and one that completely hits the photodiode, for a range of disk rotation frequencies f. From the gradient of the shown linear fit through the origin, I estimated the beam radius ω_0 according to equation 5.7 to be $7.2\,\mu\text{m}$. This represents no improvement over the measurements in section 5.5.1. If vibrations were present in the addressing system, we would expect T to fall below this line at higher rotational frequencies. At very high frequencies, the measured values of T stop decreasing, likely due to the response time of the photodiode. I conclude if the larger than expected beam spot size is an artifact of vibrations in the beam, then these vibrations have a period more than $\sim 2\,\mu\text{m}$, or a frequency greater than 50 kHz.

5.6 Conclusion

This measured value of $\omega = 7.2\,\mu\text{m}$ is much larger than the predicted value from section 5.3 of $\omega = 1.1\,\mu\text{m}$, and is comparable to the measurements made in section 5.5.1 of $3.7\,\mu\text{m} < \omega_0 < 10.2\,\mu\text{m}$. This is troubling. I have ensured that I am measuring the true narrowest point of the beam, and have done my utmost to build the system according to the design given in table 5.3. By using the spinning disk, I have tried to avoid errors due to vibrations of the system. By using the Chiral Photonics fanout I have tried to ensure the highest possible quality of input beam.

Thus the remaining source of error is that endface of the MC-PCF is damaged or poorly cut, leading to a very low quality addressing beam. If dirt attaches itself to the end of the cores, gets trapped inside the air spaces between cores, or if the ends or bodies of the cores are damaged, then light within the cores could enter modes other than the fundamental mode, or experience spatially varying phase shifts. Such a variable source a error would explain the large difference in the measured values of ω_0 at the ions by different methods and for different cores. In section 4.3 I managed to cut cleanly the MC-PCF in order to measure the high quality beams depicted in figure 4.4. As it transpires, this is not an easily repeatable task. Future work is required to reliably cut and protect the MC-PCF endface. It is hoped that if this is achieved, then the addressing system will work as designed.

Figure 5.19 shows an example of a poor quality mode, visualised using the Beam Profiler used in section 4.3. It shows clearly a strong contribution from a higher order mode, with an array of intensity peaks. This is much worse than the beam that was achieved in section 4.3, that was used to estimate the beam divergence and thus to design the addressing system. Figure 5.20 shows a similar simulated mode, and the results it would give under the knife edge procedure used in section 5.5.1. The spot size is much broader than for the mode quality simulated in section 5.3, and comparable to the measurements in section 5.5.

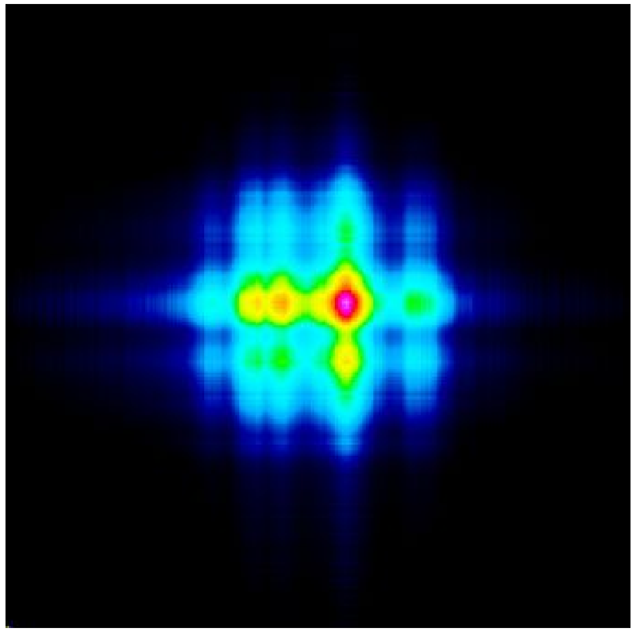

Figure 5.19: Shown is a qualitative image of the beam from the endface of the MC-PCF, where the input beam is given using the Chrial Photonics fanout. Clearly visible are higher order modes than the fundamental modes, different to the good quality mode achieved in figure 4.4. Since I am confident of a good quality input mode, I believe these modes are due to damage to the MC-PCF, either along its length, or more probably at its bare end

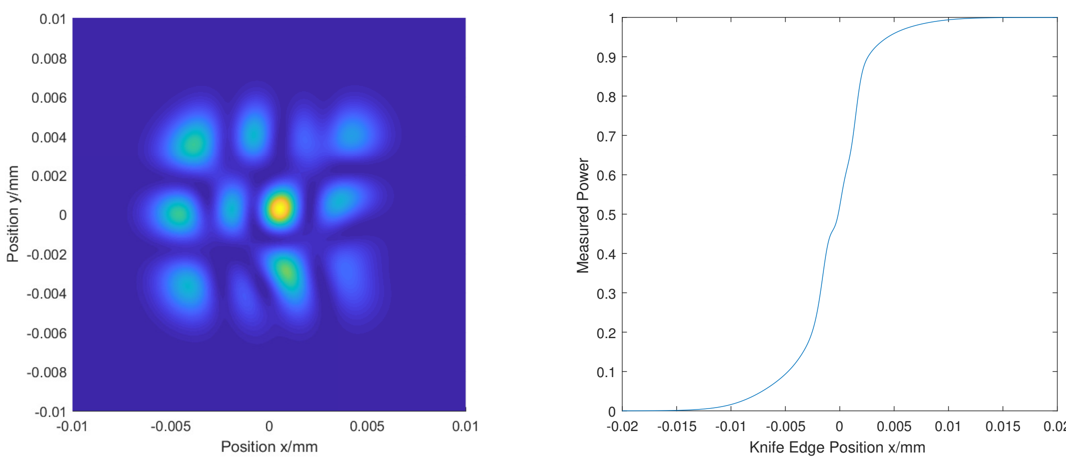

(a) (b)

Figure 5.20: Shown in figure 5.20a is a simulated mode close to the MC-PCF, qualitatively comparable to that depicted in figure 5.19. Figure 5.20b shows a knife edge measurement of such at mode in the ion plane, after it has passed through the addressing system. It gives a spot radius of $\omega = 5.8\,\mu\text{m}$, which is comparable to the results measured in section 5.5. This depends strongly on the exact choice of input mode.

Chapter 6

Summary and Outlook

Through this masters project and thesis, I have designed a system to perform single ion addressing on a string of trapped ions contained within a linear trap as part of the eQual project in the TIQI group at ETH Zürich. It was required that individually controllable beams of 400 nm light be focused onto each ion. High intensity beams at the ions was desired to minimise the time required for quantum gates. Low crosstalk between beams was desired such that the system might contribute towards a fault tolerant quantum computer.

Most aspects of this project were successful. Methods were proposed and built to efficiently divide a single laser source into multiple beams, to control each beam, and to couple each beam into the cores of an Multicore Photonic Crystal Fibre (MC-PCF). The beam profile emitted from this MC-PCF was characterised, and a system of optics was designed to focus these beams onto the ions. Under simulation, this system produced a focused spot at the ions that was as small as was allowed by the geometry of the ion trap, and that gave acceptable levels of crosstalk between ions. The system was also compatible with the individual imaging of the ions, a method for which was also proposed.

The system was built and measurements were taken in an effort to characterise the size of the addressing beams at the ions. In practice it was found to be an order of magnitude larger than the expected values. Steps were taken to eliminate sources of error, such as external vibrations, misalignments in the optical system and poor coupling into the cores of the MC-PCF. This did not result in significant improvement. The causes of the discrepancy between the simulated and measured results thus remain poorly understood. The large variance in the measured results, combined with a closer analysis of the mode structure of the MC-PCF, lead me to conclude that the quality of beam produced by the MC-PCF is dependent on the state of the MC-PCF, which in turn is very difficult to cleave reliably and very vulnerable to physical damage.

Future improvements might be made through greater understanding of the use and optical mode structure of photonic crystal fibres. The use of a photonic crystal fibre was motivated in part by the hope that the propagation of light through such a fibre would filter out higher order modes, and this initially appeared to be true, although it was difficult to reproduce this initial quality.

The long term goal is to build a scalable and stable method by which to address multiple ions. It has thus been proposed to in future dispense with the MC-PCF as part of the eQual experiment. A component similar to that used to couple light into the MC-PCF, known as a PROFA, has been ordered from Chiral Photonics. It can instead be used to project light directly onto the ions via a single objective lens, also taking inputs from many single fibres. This has the advantage that it can be mounted close to the ions inside the cryostat, which would provide stable addressing, as vibrations in the cryostat would affect the ions and the addressing beams equally, although it would no longer overlap with the imaging system, as is the case in the model I proposed. Nonetheless, though it was not entirely successfuly, the work done in this thesis contributes towards the overall eQual project and informs decisions that might be made in its future.

Bibliography

[1] Richard P. Feynman. Simulating physics with computers. *International Journal of Theoretical Physics*, 21(6):467–488, Jun 1982.

[2] Lov K. Grover. A fast quantum mechanical algorithm for database search. In *Proceedings of the Twenty-eighth Annual ACM Symposium on Theory of Computing*, STOC '96, pages 212–219, New York, NY, USA, 1996. ACM.

[3] Peter W. Shor. Polynomial-time algorithms for prime factorization and discrete logarithms on a quantum computer. *SIAM Review*, 41, 05 1997.

[4] IBM Q. *IBM Quantum Experience*, 2018.

[5] Chao Song, Kai Xu, Wuxin Liu, Chui-ping Yang, Shi-Biao Zheng, Hui Deng, Qiwei Xie, Keqiang Huang, Qiujiang Guo, Libo Zhang, Pengfei Zhang, Da Xu, Dongning Zheng, Xiaobo Zhu, H. Wang, Y.-A. Chen, C.-Y. Lu, Siyuan Han, and Jian-Wei Pan. 10-qubit entanglement and parallel logic operations with a superconducting circuit. *Phys. Rev. Lett.*, 119:180511, Nov 2017.

[6] John Clarke and Frank K. Wilhelm. Superconducting quantum bits. *Nature*, 453:1031, Jun 2008.

[7] D. Leibfried, R. Blatt, C. Monroe, and D. Wineland. Quantum dynamics of single trapped ions. *Rev. Mod. Phys.*, 75:281–324, Mar 2003.

[8] R. Marx, A. F. Fahmy, John M. Myers, W. Bermel, and S. J. Glaser. Approaching five-bit nmr quantum computing. *Phys. Rev. A*, 62:012310, Jun 2000.

[9] Ludwig E. de Clercq, Hsiang-Yu Lo, Matteo Marinelli, David Nadlinger, Robin Oswald, Vlad Negnevitsky, Daniel Kienzler, Ben Keitch, and Jonathan P. Home. Parallel transport quantum logic gates with trapped ions. *Phys. Rev. Lett.*, 116:080502, Feb 2016.

[10] F. M. Leupold, M. Malinowski, C. Zhang, V. Negnevitsky, A. Cabello, J. Alonso, and J. P. Home. Sustained state-independent quantum contextual correlations from a single ion. *Phys. Rev. Lett.*, 120:180401, May 2018.

[11] Michael A. Nielsen and Isaac L. Chuang. *Quantum Computation and Quantum Information*. Cambridge University Press, New York, NY, USA, 10th edition, 2011.

[12] DiVincenzo David P. The physical implementation of quantum computation. *Fortschritte der Physik*, 48(911):771–783, Mar 2000.

[13] Florian Leopold. *Bang-bang Control of a Trapped-Ion Oscillator*. PhD thesis, ETH Zürich, 2015.

[14] U G Poschinger, G Huber, F Ziesel, M Dei, M Hettrich, S A Schulz, K Singer, G Poulsen, M Drewsen, R J Hendricks, and F Schmidt-Kaler. Coherent manipulation of a 40 ca + spin qubit in a micro ion trap. *Journal of Physics B: Atomic, Molecular and Optical Physics*, 42(15):154013, 2009.

[15] Manuel Zeyen. Focused Raman Beam Addressing for a Trapped-Ion Quantum Processor. Master's thesis, ETH Zürich, 2016.

[16] T. Ruster, C. T. Schmiegelow, H. Kaufmann, C. Warschburger, F. Schmidt-Kaler, and U. G. Poschinger. A long-lived zeeman trapped-ion qubit. *Applied Physics B*, 122(10):254, Sep 2016.

[17] H. Sawamura, K. Kanda, R. Yamazaki, K. Toyoda, and S. Urabe. Optimum parameters for sideband cooling of a 40ca+ ion. *Applied Physics B*, 93(2):381–388, Nov 2008.

[18] Christopher J. Foot. *Atomic Physics*. Oxford University Press, 2005.

[19] D.F.V. James. Quantum dynamics of cold trapped ions with application to quantum computation. *Applied Physics B*, 66(2):181–190, Feb 1998.

[20] Emanuel Knill. Quantum computing. *Nature*, 463:441 EP –, Jan 2010.

[21] S. Debnath, N. M. Linke, C. Figgatt, K. A. Landsman, K. Wright, and C. Monroe. Demonstration of a small programmable quantum computer with atomic qubits. *Nature*, 536:63 EP –, Aug 2016.

[22] Kenneth R. Brown, Jungsang Kim, and Christopher Monroe. Co-designing a scalable quantum computer with trapped atomic ions. *Npj Quantum Information*, 2:16034 EP –, Nov 2016. Review Article.

[23] H. C. Nägerl, D. Leibfried, H. Rohde, G. Thalhammer, J. Eschner, F. Schmidt-Kaler, and R. Blatt. Laser addressing of individual ions in a linear ion trap. *Phys. Rev. A*, 60:145–148, Jul 1999.

[24] A.E. Siegman. *Lasers*. University Science Books, 1986.

[25] P. F. Moulton. Spectroscopic and laser characteristics of ti:al2o3. *J. Opt. Soc. Am. B*, 3(1):125–133, Jan 1986.

[26] G. D. Boyd and D. A. Kleinman. Parametric interaction of focused gaussian light beams. *Journal of Applied Physics*, 39(8):3597–3639, 1968.

[27] E. Hecht. *Optics*. Addison-Wesley, 4th edition, 1998.

[28] H. Eklund, A. Roos, and S. T. Eng. Rotation of laser beam polarization in acousto-optic devices. *Optical and Quantum Electronics*, 7(2):73–79, Mar 1975.

[29] D. Gloge. Weakly guiding fibers. *Appl. Opt.*, 10(10):2252–2258, Oct 1971.

[30] D. Marcuse. Loss analysis of single-mode fiber splices. *The Bell System Technical Journal*, 56(5):703–718, May 1977.

[31] Jonathan C. Knight. Photonic-crystal fibers. *Nature*, 24(424):847, Aug 2003.

[32] Philip St.J. Russell. Photonic-crystal fibers. *J. Lightwave Technol.*, 24(12):4729–4749, Dec 2006.

[33] W. J. Wadsworth, R. M. Percival, G. Bouwmans, J. C. Knight, T. A. Birks, T. D. Hedley, and P. S. J. Russell. Very high numerical aperture fibers. *IEEE Photonics Technology Letters*, 16(3):843–845, March 2004.

[34] J. C. Knight, T. A. Birks, P. St. J. Russell, and J. P. de Sandro. Properties of photonic crystal fiber and the effective index model. *J. Opt. Soc. Am. A*, 15(3):748–752, Mar 1998.

[35] Kwang N. Park and Kyung S. Lee. Improved effective-index method for analysis of photonic crystal fibers. *Opt. Lett.*, 30(9):958–960, May 2005.

[36] T. A. Birks, J. C. Knight, and P. St. J. Russell. Endlessly single-mode photonic crystal fiber. *Opt. Lett.*, 22(13):961–963, Jul 1997.

[37] E. A. J. Marcatili. Slab-coupled waveguides. *The Bell System Technical Journal*, 53(4):645–674, April 1974.

[38] P. Kaiser and H. W. Astle. Low-loss single-material fibers made from pure fused silica. *The Bell System Technical Journal*, 53(6):1021–1039, July 1974.

[39] Didier Neveux. Photochromic effect in germanosilicate fibers at very low intensities in the blue-green domain. *Appl. Opt.*, 32(21):3952–3958, Jul 1993.

[40] J. J. Koponen, M. J. Söderlund, H. J. Hoffman, and S. K. T. Tammela. Measuring photodarkening from single-mode ytterbium doped silica fibers. *Opt. Express*, 14(24):11539–11544, Nov 2006.

[41] G. R. Atkins and A. L. G. Carter. Photodarkening in tb3+-doped phosphosilicate and germanosilicate optical fibers. *Opt. Lett.*, 19(12):874–876, Jun 1994.

[42] L. J. Poyntz-Wright, M. E. Fermann, and P. St. J. Russell. Nonlinear transmission and color-center dynamics in germanosilicate fibers at 420–540 nm. *Opt. Lett.*, 13(11):1023–1025, Nov 1988.

[43] L. J. Poyntz-Wright and P. S. J. Russell. Spontaneous relaxation processes in irradiated germanosilicate optical fibres. *Electronics Letters*, 25(7):478–480, March 1989.

[44] M. Josephine Yuen. Ultraviolet absorption studies of germanium silicate glasses. *Appl. Opt.*, 21(1):136–140, Jan 1982.

[45] W. Klaus, J. Sakaguchi, B. J. Puttnam, Y. Awaji, N. Wada, T. Kobayashi, and M. Watanabe. Free-space coupling optics for multicore fibers. *IEEE Photonics Technology Letters*, 24(21):1902–1905, Nov 2012.

[46] V. I. Kopp, J. Park, M. Wlodawski, J. Singer, D. Neugroschl, and A. Z. Genack. Pitch reducing optical fiber array and multicore fiber for space-division multiplexing. In *2013 IEEE Photonics Society Summer Topical Meeting Series*, pages 99–100, July 2013.

[47] Victor I. Kopp, Jongchul Park, Mitchell Wlodawski, Eric Hubner, Jonathan Singer, Dan Neugroschl, and Azriel Genack. Vanishing core optical waveguides for coupling, amplification, sensing, and polarization control. In *Advanced Photonics*, page SoW1B.3. Optical Society of America, 2014.

[48] M Born and E Wolf. *Principles of Optics*. Cambridge University Press, 7 edition, 1999.

[49] Regina Lechner, Christine Maier, Cornelius Hempel, Petar Jurcevic, Ben P. Lanyon, Thomas Monz, Michael Brownnutt, Rainer Blatt, and Christian F. Roos. Electromagnetically-induced-transparency ground-state cooling of long ion strings. *Phys. Rev. A*, 93:053401, May 2016.